Final Report for NASA Grant NAG-1-1103

NUMERICAL SIMULATION OF STABILITY AND STABILITY CONTROL OF HIGH SPEED COMPRESSIBLE ROTATING COUETTE FLOW

Principal Investigator: Dr. Sedat Biringen
Phone : (303)492-2760
FAX : (303)492-7881

Research Associate: Dr. Ferhat F. Hatay
Phone : (303)492-3939
FAX : (303)492-7881

Department of Aerospace Engineering Sciences
University of Colorado
Boulder, Colorado 80309

NASA Technical Monitor: Dr. William E. Zorumski
Acoustics Division

ABSTRACT

The nonlinear temporal evolution of disturbances in compressible flow between infinitely long, concentric cylinders is investigated through direct numerical simulations of the full, three-dimensional Navier-Stokes and energy equations. Counter-rotating cylinders separated by wide gaps are considered with supersonic velocities of the inner cylinder. Initially, the primary disturbance grows exponentially in accordance with linear stability theory. As the disturbances evolve, higher harmonics and subharmonics are generated in a cascading order eventually reaching a saturation state. Subsequent highly nonlinear stages of the evolution are governed by the interaction of the disturbance modes, particularly the axial subharmonics. Nonlinear evolution of the disturbance field is characterized by the formation of high-shear layers extending from the inner cylinder towards the center of the gap in the form of jets similar to the ejection events in transitional and turbulent wall-bounded shear flows.

1 INTRODUCTION

The interaction of viscous and centrifugal mechanisms in the stability of high-speed shear flows can be studied in a relatively simple model offered by the compressible rotating Couette flow. In the present work, direct numerical simulations are performed to investigate the nonlinear temporal evolution of forced disturbances in wide gaps between counter-rotating, concentric cylinders of infinite length.

The balance of viscous and centrifugal forces determines the first transition in the incompressible Couette flow which can be predicted by the linear stability theory.[1] Further interaction of these two mechanisms generates rich complex flow patterns[2] which render the problem attractive but the ensuing nonlinearities are hardly amenable to a thorough theoretical treatment. According to Stuart[3] nonlinear effects can be the generation of harmonics (and subharmonics) of the fundamental mode, distortion of the mean motion, and the distortion and evolution of the fundamental mode as well as of the other modes. Finite-amplitude incompressible Taylor-Couette flow has been treated in the vicinity of the neutral-stability region by Davey[4] by weakly-nonlinear methods based on the amplitude-expansion procedures suggested by Stuart.[5] One critical assumption used by Davey is that all harmonics of axial periodicity add in phase. Snyder and Lambert[6] demonstrated in their experiments that all harmonics are indeed in phase with the fundamental resulting in the emergence of jets in the flow field as a direct consequence of nonlinear interactions. Nonlinear jet-modes were also identified by Lorenzen, Pfister & Mullin[7] in the experiments of incompressible Taylor-Couette flow

with a stationary outer cylinder.

Weakly nonlinear theories consider a subset of nonlinear effects, include a limited number of modes and are often restricted to the proximity of the region where the disturbances are only marginally unstable. Among such studies, Jones[8,9] used a mixed finite-difference/spectral technique to study the nonlinear incompressible Taylor-Couette flow effectively for Reynolds numbers (or Taylor numbers) well beyond the critical values. He found the jet-mode to be the most unstable nonlinear mode as opposed to the classical wavy mode for some parameter ranges. Jones also found two distinct modes, i.e. the harmonic and subharmonic jet-modes. The subharmonic mode is slightly more unstable; therefore the harmonic mode has not been detected in experiments.

The study of compressible flow instabilities is more complicated than the incompressible ones because disturbances in density, temperature, viscosity and conductivity have to be considered in addition to pressure and velocity fluctuations.[10] Hatay *et al.*[11] studied the linear stability of compressible Taylor-Couette flow at finite Mach numbers for three-dimensional disturbances. Accordingly, compressibility can either stabilize or destabilize the growth of small-amplitude disturbances depending on the gap width and the rotational speeds of the cylinders. By solving the fully nonlinear, compressible equations, the present study aims at extending the previous results from the linear theory including all possible nonlinear effects in a parameter range where the disturbances are predicted to be linearly most unstable.

2 GOVERNING EQUATIONS

We consider viscous compressible flows governed by the Navier-Stokes and energy equations and the thermodynamic equation of state. These equations are written for a heat conducting perfect gas in a three-dimensional cylindrical coordinate system, (r,θ,z) denoting radial, azimuthal and axial directions respectively. The flow field is bounded by two infinitely-long, concentric cylinders; we define R as the radius and Ω as the angular velocity of the cylinders (Figure 1). Subscript $()_1$ refers to the inner cylinder and subscript $()_2$ to the outer cylinder; superscript $()^*$ is used for dimensional quantities. Scalar flow variables are density ρ, temperature T, and pressure p and the velocity vector is denoted by $\mathbf{u} = (u_r, u_\theta, u_z)$. Length, time, velocity, density, pressure and temperature are scaled with R_1^*, Ω_1^{*-1}, $\Omega_1^* R_1^*$, ρ_1^*, $\rho_1^*(R_1^*\Omega_1^*)^2$ and T_1^* respectively. Thermophysical properties, viscosity and heat conductivity (μ^* and k^*), are also scaled with their respective values on the surface of the inner cylinder.

The governing equations can be expressed in terms of the dimensionless variables in vector form as follows:

$$\frac{\partial \rho}{\partial t} + \nabla \cdot (\rho \mathbf{u}) = 0, \tag{1}$$

$$\frac{\partial \rho \mathbf{u}}{\partial t} + \nabla \cdot (\rho \mathbf{u}\mathbf{u}) = -\nabla p + \frac{1}{Re}\nabla \cdot \boldsymbol{\tau}, \tag{2}$$

$$\frac{\partial E_T}{\partial t} + \nabla \cdot (E_T \mathbf{u}) + \frac{1}{(\gamma-1)M^2}\frac{1}{RePr}\nabla \cdot (\mu \nabla T) = \frac{1}{Re}\nabla \cdot (\boldsymbol{\tau}\mathbf{u}) - \nabla \cdot (p\mathbf{u}) \tag{3}$$

$$\gamma M^2 p = \rho T, \tag{4}$$

where

$$\boldsymbol{\tau} = \mu(\nabla \mathbf{u} + \nabla \mathbf{u}^T) + \lambda(\nabla \cdot \mathbf{u})\mathbf{I}. \tag{5}$$

is the viscous stress tensor and $\lambda = -2/3\mu$ is the second coefficient of viscosity; $()^T$ is the transpose operator, and $\mathbf{I}$ is the identity tensor. Total energy is the sum of kinetic and internal energies:

$$E_T = \rho\left(\frac{T}{\gamma(\gamma-1)M^2} + \frac{\mathbf{u}\cdot\mathbf{u}}{2}\right). \tag{6}$$

Reynolds number, Mach number and Prandtl number above are defined as:

$$Re = \frac{\Omega_1^* R_1^{*2}}{\mu_1^*/\rho_1^*}, \quad M = \frac{R_1^*\Omega_1^*}{\sqrt{\gamma \mathrm{R}^* T_1^*}}, \quad Pr = \frac{\mu_1^* c_p^*}{k_1^*}, \tag{7}$$

where $\mathrm{R}^* = c_p^* - c_v^*$ is the gas constant. Variation of Prandtl number Pr, and specific heats c_p^*, c_v^* with temperature is neglected. In this study Pr and specific heat ratio γ=c_p^*/c_v^* are taken to be 0.7 and 1.4 respectively. Sutherland's law is used to express the dependency of viscosity μ on temperature,

$$\mu = k = T^{\frac{3}{2}}\frac{1+S}{T+S}, \tag{8}$$

where $S = 110.4K/T_1^*$ and $T_1^* = 288.15K$.

No-slip velocities and prescribed temperatures are imposed along the radial direction on the cylinder surfaces. The boundary conditions for the pressure are obtained from the radial momentum equation. Periodicity is assumed in the azimuthal, θ, and the axial, z, directions. The assumption of axial-periodicity is equivalent to following the evolution of disturbances in time with respect to a reference frame moving with the phase (or group) velocity of the disturbances. Consequently, the computational box-length

corresponds to the largest wavelength represented in the solution. The choice of the box-length is not a trivial task as the most critical waves should be included in the simulation. For this purpose, results from an earlier linear stability analysis of this problem[11] were used to determine the wavelength of the most critical disturbances.

The base flow is a steady solution of the governing equations. For this purpose, axisymmetric two-dimensional flow in the (r,θ) plane is assumed so that all variables depend only on the radial coordinate, r. Velocity components in the axial direction, z, and the radial direction, r, are taken to be zero for a purely azimuthal base flow. The resulting system of ordinary differential equations are then solved as a boundary value problem.[11]

The general form of the initial distributions of the flow variables used in the simulations is:

$$\Phi(r,\theta,z,t=0) = \Phi_0 + A_1\Phi_1 + A_2\Phi_2 + A_R\Phi_R, \tag{9}$$

where $\Phi = (\rho, \rho u_r, \rho u_\theta, \rho u_z, E_T)^T$ is the vector of primary variables, and the base flow is denoted by Φ_0. The primary disturbance, Φ_1 is obtained from the least-damped linear, complex eigensolution, $\hat{\Phi}_1$ with a maximum amplitude of A_1:

$$\Phi_1 = Real\left[\hat{\Phi}_1(r)\exp[i(\alpha z + \beta\theta)]\right], \tag{10}$$

where α and β are the wavenumbers in the z and θ directions, respectively, and $i = \sqrt{-1}$. The axial subharmonic of the primary disturbance is similarly obtained from the linear stability analysis as $\hat{\Phi}_2$ with the wavenumber pair $(\alpha/2, \beta)$ and is introduced with a maximum amplitude of A_2 into the initial

field:

$$\Phi_2 = Real\left[\hat{\Phi}_2(r)\exp\left(i(\frac{\alpha}{2}z+\beta\theta)\right)\right], \tag{11}$$

Note that zero phase is used for Φ_1 and Φ_2 in Equations 10 and 11. A random field, Φ_R at a maximum amplitude of A_R is also added to the initial disturbance fields to trigger the nonlinear evolution of the instabilities. The random field is generated in the physical space by using random number generators provided by the Cray Scientific and Mathematical Functions Library.

The computational domain length in the axial direction, L_z, is specified as $2\pi/\alpha$ in the harmonic simulations and as $4\pi/\alpha$ when the evolution of axial-subharmonics is investigated.

3 NUMERICAL METHOD

The solution procedure used in the present work is the Two-Four method proposed by Gottlieb & Turkel[12] as a fourth-order variant of the fully-explicit MacCormack method. The Two-Four scheme is highly phase-accurate and is very suitable for wave propagation and wave interaction problems.[13] In the present work, the Two-Four method is adapted to the cylindrical geometry with a source-like treatment of the centrifugal terms. A stretched mesh in the r direction is used to cluster more nodes towards the solid walls. The allowable time step, Δt, for the current fully explicit method depends on the Courant Number (CFL) which is defined as:

$$CFL = \Delta t \max_{grid}\left[\frac{|u_r|}{\Delta r}+\frac{|u_\theta|}{r\Delta\theta}+\frac{|u_z|}{\Delta z}+a\sqrt{\frac{1}{\Delta r^2}+\frac{1}{(r\Delta\theta)^2}+\frac{1}{\Delta z^2}}\right.$$

$$+ 2\frac{vis}{Re}\left(\frac{1}{\Delta r^2} + \frac{1}{(r\Delta\theta)^2} + \frac{1}{\Delta z^2}\right)\Bigg], \tag{12}$$

where the term vis is given as,

$$vis = \frac{\max\left(\mu, \lambda + 2\mu, \frac{\gamma\mu}{Pr}\right)}{\rho}, \tag{13}$$

and a is the local speed of sound,

$$a = \sqrt{\frac{\gamma p}{\rho}}. \tag{14}$$

The stability of the numerical scheme is ensured for $CFL \leq 1$ and the scheme is optimized for $CFL \approx 2/3$.

The solution procedure was implemented on the CRAY-YMP at NASA Langley Research Center taking full advantage of the vector architecture of this processor. It is desired that in the absence of disturbances, the base flow should satisfy the discretized full governing equations to the order of machine accuracy available by the computing platform. In the present problem, this is achieved by introducing extra source terms (which represent the base flow) into the discrete form of the θ-momentum and total energy, E_T, equations. These source terms are calculated simply as the difference between the left and right-hand sides of the discrete equations (typically of order 10^{-12}) and are kept constant thereafter throughout the computation. This technique was applied by Erlebacher & Hussaini[14] in their simulations of supersonic boundary-layer flow. For the present flow field, this operation is equivalent of obtaining fully nonlinear, complete perturbation equations, hence the behavior of the system with or without the source terms does not change in any way.

4 RESULTS

4.1 Initial Disturbances

The Navier-Stokes solver described in Section 4 was tested extensively by comparisons with the linear theory; these results are reported elsewhere.[11] Accordingly, the amplitude and phase agreement between the linear theory and the direct numerical simulation is better than 1.0%.

In the present work, we investigate the nonlinear temporal evolution of compressible flow in a wide gap ($R_1/R_2 = 0.5$) between infinitely-long, concentric cylinders with equal and opposite rotation speeds ($\Omega_2/\Omega_1 = -1$). Direct numerical simulations were performed at a supersonic Mach number of $M = 2.0$ and at a Reynolds number of $Re = 2,000$. According to the linear stability analysis[11] the primary instability is a three-dimensional, traveling wave when the cylinders are in the counter-rotating configuration at finite Mach numbers. At $Re = 2,000$ a wide band of linearly unstable disturbances exist with different axial and azimuthal wavenumbers (α, β) and the combination of $\alpha = 19.0$ and $\beta = 1$ gives the highest growth rate; due to the circular geometry, β can assume only integer values. For these parameter values, a high-resolution linear analysis with 121 nodes in the radial direction generates the temporal eigenvalue (complex frequency) $\omega = 0.5168 + i0.9758$, whose imaginary part is the growth rate. The corresponding eigenfunctions (Figure 2) were used as the primary disturbance field ($\hat{\Phi}_1$ in Eq. 11) for the Navier-Stokes simulations and reveal a one-cell structure with maxima closer to the inner cylinder and quiescent behavior in the outer half of the domain. The eigenfunctions for the axial subharmonic ($\hat{\Phi}_2$ in Eq. 11) were obtained

in a similar manner and are presented in Figure 3.

In the subsequent sections, we report the results from three separate direct numerical simulations. The first simulation discloses the evolution of the harmonics in the absence of the subharmonic generation, whereas the second allows for the evolution of the subharmonics. The last simulation is initialized with comparable finite amplitudes of the primary and axial-subharmonic disturbances with zero phase difference, revealing the effects of forced subharmonics. We analyze the nonlinear development of the disturbance field for each case.

4.2 Harmonic Development

This simulation was initialized with the primary disturbance imposed on the base flow with a maximum amplitude of $A_1 = 10^{-3}$ together with a random disturbance field of amplitude $A_R = 10^{-6}$. The computational domain was chosen to accommodate one full axial wavelength of the fundamental disturbance ($L_z = 2\pi/\alpha$). The temporal evolution of the disturbances was then studied with a computational grid resolution of $65 \times 66 \times 34$ in the radial, azimuthal, and axial directions, respectively. During the course of the simulation, the solution fields were interpolated onto a high-resolution grid of $65 \times 66 \times 66$ and integrated in time at this resolution. The complete agreement between these two simulations indicate that solutions are grid independent.

In order to analyze the data, we first performed one-dimensional Fourier expansions in one periodic direction (either θ or z) and followed the time evolution of the maximum Fourier amplitudes. For example, an expansion

of the field variable ϕ in a one-dimensional Fourier series along the axial direction, z, can be written as:

$$\phi(r,z,\theta,t) = \sum_{k_1} \hat{\phi}(r,k_1,\theta,t) \exp(ik_1\alpha z), \tag{15}$$

where $|k_1| < \frac{1}{2}N_z$ and N_z is the number of nodes in the z direction. The maximum amplitude is found in the (r,θ) plane:

$$A(k_1,t) = \max_{(r,\theta)} \quad (\hat{\phi}\hat{\phi}^*), \tag{16}$$

where $()^*$ denotes the complex conjugate. Similarly, a one-dimensional Fourier expansion in the azimuthal direction , θ, yields:

$$\phi(r,z,\theta,t) = \sum_{k_2} \hat{\phi}(r,z,k_2,t) \exp(ik_2\beta\theta), \tag{17}$$

where $|k_2| < \frac{1}{2}N_\theta$ and N_θ is the number of nodes in the θ direction. This time, the maximum amplitude is found in the (r,z) plane:

$$A(k_2,t) = \max_{(r,z)} \quad (\hat{\phi}\hat{\phi}^*). \tag{18}$$

As predicted by the linear theory, the initial growth of the primary disturbance is exponential. In Figure 4, the time evolution of $A(k_1 = 1,t)$ and $A(k_2 = 1,t)$ is compared with the linear theory. The quantitative comparison of the growth rates in Table 1 reveals good agreement in the initial stage.

The time history of $A(k_1,t)$ and $A(k_2,t)$ is presented in Figure 5 for the total energy, E_T. In each of these plots, the topmost curve represents the first wavenumber ($k_1 = 1$ or $k_2 = 1$ in Eq. (16)) and the lower curves are the harmonics in ascending order. The amplitudes of the harmonics first

decay and then are energized and follow the rapid growth of the primary mode. The excitation of the harmonics takes place in a perfect hierarchy in which the smallest wavenumber becomes energized first, reaches saturation at a finite amplitude and then transfers its excess energy to the next smaller wavenumber. This cascading process continues until all the modes reach a nonlinearly quasi-saturated *plateau* stage along which the disturbances are sustained at finite amplitudes. The whole range of harmonics, not a few wavenumbers, in both the axial and azimuthal directions is supported in this stage. Power spectra of A, the maximum amplitude of the total energy E_T as defined in Eqs. (16) and (17), at $t = 25.51$ (Figure 6) are smooth and continous with a fast decay towards the large wavenumbers indicative of the sufficient grid resolution used in the numerical solution at this stage. The smoothness of the spectra is related to the continous cascade of energy from the smaller wavenumbers.

Figure 7 illustrates the generation of the harmonics in the two-dimensional wavenumber space. Here, E_T is expanded in a Fourier series in θ and z directions as:

$$E_T(r,z,\theta,t) = \sum_{k_1}\sum_{k_2} \hat{E}_T(r,k_1,k_2,t)\exp\left(ik_1\alpha z + ik_2\beta\theta\right), \qquad (19)$$

where $|k_1| < \frac{1}{2}N_z$, $|k_2| < \frac{1}{2}N_\theta$, N_z and N_θ are the number of nodes in z and θ directions, respectively. The amplitude of these modes are defined as:

$$A(k_1,k_2,t) = \frac{1}{R_2 - R_1}\int_{R_1}^{R_2} \hat{E}_T \hat{E}_T^{\,*}\, dr. \qquad (20)$$

In the present analysis, the quantity given by Eq. (20) refers to the energy contained in the spectral mode (k_1, k_2). This definition of modal energy is not

unique and differs from the incompressible definition. However, the present approach has the advantage of containing both the kinetic and internal energies of the disturbance fields. Moreover, the analysis based on the present definition gives a coherent and consistent picture of the events in the physical space as well as in the spectral space.

As depicted in Figure 5, the harmonics are energized sequentially as time progresses. Also, new peaks appear in the two-dimensional Fourier spectrum shown in Figure 7 in a systematic fashion along the axial-harmonics. The direction of this hierarchial generation of harmonics is initially:

$$(n\alpha, n\beta) \rightarrow [(n+1)\alpha, (n+1)\beta] \tag{21}$$

where $n = 1, 2, ...\frac{1}{2}N_z$. Once the harmonics are energized in this hierarchy, energy is transferred to the other wavenumbers in the two-dimensional wavenumber space. At later times, a uniform distribution of the amplitudes is approached with gradual decay towards the smaller wavenumbers. It is interesting to note that the amplitude-decay is much slower in the azimuthal direction than in the axial direction. Therefore, the azimuthal mesh resolution requirements became prohibitive beyond $t = 40.0$.

The main energy source in this temporal evolution is the external torque applied at the rotating cylinders. Figure 8 presents the mean velocities (averaged in the z-θ plane) at selected times. The increase in the gradients close to the inner cylinder is due to more efficient energy and momentum transfer. Relatively flat portions of the u_θ profiles for about $r \approx 1.1$ indicate enhanced momentum-mixing in that region. The development of non-zero u_r and u_z is related to the nonlinear distortions of the initially sinusoidal disturbance

fields. Consequently, in the inner half of the gap, the mean flow is no longer purely azimuthal but has a weakly swirling component.

The events in the spectral and physical spaces can be interconnected through the inspection of instantaneous disturbance fields. Figure 9 presents contour plots of disturbance total energy, E_T, in several (r-z) planes. During the early stage, $t = 0.6313$, the initially imposed randomness quickly dies and the fundamental mode with its characteristic sinusoidal variation dominates the flow field at this cross-section. At later times, as the harmonics are energized and the plateau stage is reached, the formation of a jet-like structure is observed close to the inner wall. The harmonics are generated in phase with each other; consequently, their superposition leads to this high-shear-layer formation. The jet-like structure expands towards the center of the gap in the shape of a mushroom but does not quite extend into the outer half of the gap so that this region remains stable. Along the plateau stage ($t > 20$), these jets or mushroom-like ejection structures promote even higher-shear layers with stronger gradients close to the inner wall. Three-dimensional isosurfaces of disturbance total energy, E_T, at the levels of 50% of the maximum of the disturbance field, are presented in Figure 10 to illustrate this sequence of events in greater detail. In the beginning of the plateau ($t = 12.85$), the isosurfaces are perfectly spiral, indicating the dominance of the fundamental mode. The development of high shear layers is discernible in the high energy isosurface as it narrows close the inner cylinder and spreads towards the center of the channel. Along the plateau ($t = 31.72$), the jets get thinner and the structures become susceptible to the higher instability

mechanisms as evident from the waviness superimposed on the spirals. This critical wavy development in the azimuthal direction is also evident from the increasing amplitudes and the crowdening if the azimuthal spectrum for $t > 30$ in Figure 5. Eventually (t=35.48), the spiral symmetry is lost as the high energy structure locally detaches from the wall generating small-scale structures during the breakdown process. The investigation of the physics of flow transition beyond this stage would require an extremely high spatial and temporal resolution not affordable by the computer resources available for this study.

4.3 Subharmonic Development

In this simulation, the computational domain is extended to accommodate two axial-wavelengths of the fundamental disturbance ($L = 2\lambda_z = 4\pi/\alpha$) in order to allow the generation and the evolution of the axial-subharmonics of the fundamental mode. For this case, the number of nodes is increased to $81 \times 130 \times 102$ in the radial, azimuthal, and axial directions, respectively. The other parameters and the initial conditions are kept the same as in the previous harmonic simulation. The first subharmonic mode is excluded from the initial conditions ($A_2 = 0$) and can be generated only through nonlinear mechanisms.

Figure 11 depicts a similar evolution of the amplitudes of the one-dimensional Fourier components as in the harmonic case: initial rapid growth of the fundamental mode saturates to reach a plateau stage. For all the simulations performed in the present study, the nonlinear saturation is achieved over ap-

proximately one rotation of the cylinders (period $= 2\pi/\Omega_1 = 6.28$). Therefore, the mechanism for the generation and the immediate evolution of both harmonic or subharmonic disturbances must be the inviscid, rotational instabilities. As the disturbances evolve and attain finite amplitudes, a nonlinear saturation state is reached.

The evolution of the subharmonics is distinct from that of the harmonics. Starting from the small-amplitude random initial disturbance field, subharmonic modes neither reach the saturation level nor do they catch up with the harmonics until the very late stages of the transition process.

Figure 12 compares the spectral time evolution of the axial-harmonic modes from a preliminary run performed up to $t = 21$ at a resolution of $65 \times 66 \times 102$ with the $81 \times 66 \times 102$ high resolution case. This comparison reveals a similar behavior providing further justification to the adequacy of the computational grid used throughout the present study.

Figure 13 shows the radial distributions of the Fourier amplitudes for the mean flow, the fundamental mode, and the first subharmonic mode at different times. Maximum amplitudes occur close to the inner cylinder, and strong development of a secondary extremum for $r \approx 1.2$ is observed at later times. The amplitudes at the inner cylinder surface are not zero, because as the kinetic energy of the disturbances diminishes to zero, the internal energy content actually increases very rapidly in the near-wall region.

In Figure 14, the subharmonic components attain a well-developed spectrum showing the decay of energy towards higher wavenumbers. The spectra of subharmonics and harmonics are similar but separate, suggesting a dif-

ferent route for energy transfer for the subharmonics. A nonlinear energy transfer analysis can usually be instrumental in clarifying interactions between different modes[15] and can be performed by expanding the terms of the energy equation (Eq. 3) in Fourier series (Eq. 19) for the temporal evolution of the present flow. Neglecting the viscous terms because their contribution to mode interactions is secondary to the convective terms, the following equation is obtained from Eq. (19) for the nonlinear evolution of the Fourier modes:

$$\frac{\partial \hat{E}_T(r,k_1,k_2,t)}{\partial t} = -\sum_{k_1'}\sum_{k_2'} \hat{\boldsymbol{T}}(r,k_1,k_2,k_1',k_2',t) \tag{22}$$

where $\hat{\boldsymbol{T}}$ is the energy transfer rate to the mode (k_1,k_2) from (k_1',k_2') and (k_1-k_1',k_2-k_2') modes:

$$\hat{\boldsymbol{T}}(r,k_1,k_2,k_1',k_2',t) = -\nabla\cdot\Big[\hat{E}_T(r,k_1',k_2',t)\hat{\mathbf{u}}(r,k_1-k_1',k_2-k_2',t)$$

$$+\hat{p}(r,k_1',k_2',t)\hat{\mathbf{u}}(r,k_1-k_1',k_2-k_2',t)\Big]. \tag{23}$$

The interaction between the modes can now be quantified as:

$$\boldsymbol{T}(k_1,k_2,k_1',k_2',t) = \frac{1}{R_2-R_1}\int_{R_1}^{R_2} \hat{\boldsymbol{T}}(\hat{\boldsymbol{T}})^* dr. \tag{24}$$

Note that this is a positive-definite quantity and does not show the direction of transfer. The interactions of the harmonic, $(n\alpha,n\beta)$, and the axial-subharmonic, $([n-1/2]\alpha,n\beta)$, modes with the mean flow, mode (0,0), is presented in Figure 15. The evident similarity between energy transfer rates displayed in these figures and the mode amplitudes shown in Figure 14 reveals that there is a direct energy transfer to each mode from the mean flow. When

a harmonic mode reaches saturation so does its interaction with the mean flow. Along the saturation state, the mean flow continues to supply energy to the modes and the modes which reach saturation transfer their excess energy to the higher modes down the nonlinear energy cascade. In the meantime, the subharmonic modes never reach saturation and their interaction with the mean flow continously increases during the simulation.

Interactions of the fundamental mode, (α, β), with the other modes (Figure 16) indicate a similar energy transfer mechanism for the fundamental compared with the mean mode. Accordingly, the fundamental mode constitutes the next level in the harmonic cascade after the mean flow in transferring energy to the harmonic and subharmonic modes and this scenario repeats itself along the harmonic cascade. Considering all modal energy transfer combinations, when a mode reaches saturation, net energy transfer to that mode diminishes to zero as the energy cascade continues to operate in *equilibrium.*

Figure 17 displays the time evolution of the disturbance total energy, E_T, in several (r, z) sections for $\theta = 0$ and π. Following the initial exponential-growth stage, jet-like ejection structures develop as in the harmonic case. These structures occur with the periodicity of the fundamental disturbance and are indeed harmonic in nature. At later times, subharmonic structures develop and compete with the harmonics. The emergence of subharmonic structures in physical space is the result of merging adjacent ejection structures yielding a periodicity with twice the wavelength of the fundamental disturbance in the axial direction. These subharmonic jet-like structures

are stronger than their harmonic predecessors and reveal a powerful ejection extending from the wall region spreading towards the outer cylinder. The subharmonic structures quickly become susceptible to the higher instabilities leading to flow breakdown and are also accompanied by changes in the temporal response. In Figure 18, time-history data collected at a fixed point in space are presented. Quasi-periodic behavior along the plateau stage is discernible by two sequential peaks followed by two troughs with a period close to that of the fundamental mode ($2\pi/Real(\omega) = 12.16$). The disturbances have gained appreciable amplitude of about 0.05-0.10 at this stage. This temporal response is nonlinearly distorted forming spikes concurrent with the formation of jet-like structures in space. The loss of spatial symmetry takes place simultaneously with the loss of quasi-periodicity in time, indicating the end of the plateau stage.

The near-wall events investigated throughout the present study can also be traced from the the development of equishear lines at the wall. Figure 19 illustrates the development of the disturbance part of $\mu\partial u_\theta/\partial r$ at the inner cylinder wall. Initially, the equishear lines are straight with an inclination of α/β in the (z-θ) plane tracing the spiral structure imposed by the fundamental disturbance. Along the plateau stage, the formation of high-shear layers caused by the strong jet-like structures is indicated from the intensity of the equishear lines. The flow becomes susceptible to higher instability mechanisms evident from the waviness of these contours at later times and the breakdown follows the emergence of structures with higher wavenumbers.

4.4 Forced Subharmonic Development

The simulation described in Section 4.3 indicated that when subharmonics are allowed to develop in the computational box by prescribing the appropriate box-length, they may dominate over the harmonic structures. In the previous simulations, although linearly the most unstable mode was chosen as the primary disturbance, the axial-subharmonics clearly have a crucial role during the nonlinear stage. To further clarify this issue, in the third simulation we introduced the subharmonic disturbances in the initial conditions with $A_2 = 10^{-3}$ together with the harmonic disturbances ($A_1 = 10^{-3}$); a random field ($A_R = 10^{-6}$) was also imposed on the base flow.

Starting with equal amplitudes for the first subharmonic mode and the fundamental, during the exponential-growth stage (Figure 20) the axial-subharmonic modes evolve in a manner similar to the evolution of the harmonics. Both the subharmonic and the harmonic modes reach finite-amplitude levels for nonlinear saturation after approximately one rotation of the cylinders. However, the plateau stage is much less well-defined and less stable than the previous simulations and amplitudes of the azimuthal modes fluctuate along the plateau. In Figure 21 the amplitude spectra of the one-dimensional Fourier modes indicate slower decay towards the small wavenumbers compared with the previous simulations and the spectrum of the azimuthal modes is no longer smooth but contains small-scale oscillations. Consequently, the forced subharmonics appear to have a detrimental effect on the sustainability of the plateau stage.

As the amplitudes of the harmonics and subharmonics become compara-

ble, nonlinear developments lead directly to the formation of jet-like structures of the subharmonic type; no initial harmonic stage is observed during this simulation. Moreover, these structures are no longer confined to the inner half of the gap but extend further into the outer half which remained stable during the nonlinear evolution in the previous numerical simulations (Sections 4.2 and 4.3). Although the jets do not quite impinge upon the outer cylinder, they are strong enough to instigate significant activity in the outer half of the gap (Figure 22).

As in the previous case, the formation of high-shear layers is discernible from the intensification of equishear lines in the contours of the disturbance part of $\mu \partial u_\theta / \partial r$ at the inner cylinder wall (Figure 23). Characteristic of this simulation is the increasing subharmonic character of the flow field during the plateau stage. The resulting structures quickly become subject to higher instability mechanisms and lose their spiral symmetry.

In all of the cases presented in this work, sharp boundary layers form on both the outer and inner cylinder walls during the nonlinear stage; however, the ejection type events originate only close to the inner cylinder giving further indication that they are produced mainly by rotational instability mechanisms. As the nonlinear evolution progresses, rotational instabilities interact and compete with viscous instabilities. Instabilities occuring in the outer region in the forced-subharmonic case is likely to be a product of such interactions. In all stages of the evolution, compressibility maintains a recessive role and does not cause any peculiar changes in the nature of instabilities which are nurtured by viscous and centrifugal mechanisms.

5 CONCLUSIONS

Three-dimensional direct numerical simulations of the nonlinear evolution of disturbances in compressible rotating Couette flow were performed at a moderate Mach number ($M = 2.0$) and at a Reynolds number of $Re = 2000.0$. Initial conditions consisted of a random field imposed on the small-amplitude fundamental and the first axial-subharmonic modes which were obtained as three-dimensional traveling wave solutions from a high-resolution linear stability analysis.

The initial growth of the fundamental mode obtained from the present DNS is in good agreement with the linear stability predictions. The harmonics and subharmonics first decay in favor of the exponentially-growing fundamental mode and then become excited and start to grow in the order of increasing wavenumbers. The growth of the modes saturates when finite amplitudes are reached; this nonlinear saturation state is referred to as the plateau stage. When excluded from the initial conditions, the axial-subharmonics do not attain finite amplitudes to reach the plateau stage. For initial conditions that contain equal amplitude forced subharmonic and the fundamental disturbances, the subharmonics reach a nonlinearly saturated state; however, this plateau stage cannot be sustained. Our results suggest that the axial subharmonic development is the path of transition dominating the nonlinear evolution of this flow.

Along the plateau stage jet-like structures form carrying the fluid from the inner cylinder to the center of the gap. In the absence of forced subharmonics, these ejection events are harmonic structures and tend to merge to attain a

subharmonic character as they evolve. Otherwise, for forced subharmonics, subharmonic jets dominate both the inital and later stages of the transition process. The jets grow stronger and narrower and become susceptible to higher instability mechanisms. Eventually, spiral symmetries are broken by the detachment of the jets from the wall in a non-uniform manner generating small-scale structures during the process. The end of the plateau stage is also marked by the loss of quasi-periodicity in the temporal response.

The events during the transition process of this supersonic shear flow are mainly generated by the interaction of the centrifugal and viscous mechanisms which are prevalent in incompressible shear flows as well. Only indirectly does compressibility affect the essentially incompressible transition phenomena in this shear-driven flow.

References

[1] G. I. Taylor, "Stability of a viscous fluid contained between two rotating cylinders", Phil. Trans. **A 223**, 289 (1923).

[2] D. Coles, "Transition in circular Couette flow", J. Fluid Mech. **21**, 385 (1965).

[3] S. T. Stuart, "On the nonlinear mechanics of wave disturbances in stable and unstable parallel flows. part 1. the basic behavior in plane poiseuille flow", J. Fluid Mech. **9**, 353 (1960).

[4] A. Davey, "The growth of Taylor vortices in flow between rotating cylinders", J. Fluid Mech. **14**, 336 (1962).

[5] S. T. Stuart, "On the non-linear mechanics of hydrodynamic stability", J. Fluid Mech. **4**, 1 (1958).

[6] H. A. Snyder and R. B. Lambert, "Harmonic generation in Taylor vortices between rotating cylinders", J. Fluid Mech. **26**, 545 (1966).

[7] A. Lorenzen, G. Pfister, and T. Mullin, "End effects on the transition to time-dependent motion in the Taylor experiment", Phys. Fluids **26**, 10 (1982).

[8] C. A. Jones, "On flow between counter-rotating cylinders", J. Fluid Mech. **112**, 443 (1982).

[9] C. A. Jones, "The transition to wavy Taylor vortices", J. Fluid Mech. **157**, 135 (1985).

[10] L. M. Mack. "Boundary-layer linear stability theory", *Special Course on Stability and Transition of Laminar Flow*, edited by R. Michel (AGARD, Neuilly sur Seine, France, 1984), AGARD Report No. 709, p. 3-1.

[11] F. F. Hatay, S. Biringen, G. Erlebacher, and W. E. Zorumski, "Stability of high speed compressible, rotating Couette flow", Phys. Fluids **A**, **5**, 393 (1993).

[12] D. Gottlieb and E. Turkel, "Dissipative two-four methods for time-dependent problems", Math. Comput. **30**, 703 (1976).

[13] S. Biringen and A. Saati, "Comparison of several finite-difference methods", J. Aircraft **72**, 90 (1990).

[14] G. Erlebacher and M. Y. Hussaini, "Numerical experiments in supersonic boundary layer stability", Phys. Fluids **A 2**, 99 (1989).

[15] E. M. Saiki, S. Biringen, G. Danabasoglu, and C. L. Streett, "Spatial simulation of secondary instability in plane channel flow: comparison of k- and h-type disturbances", J. Fluid Mech. **253**, 485 (1993).

	Azimuthal Modes	Axial Modes	Linear Theory
ρ	0.973203	0.973227	0.975964
ρu_r	0.978329	0.978330	0.975964
ρu_θ	0.974753	0.974760	0.975964
ρu_z	0.975856	0.975860	0.975964
E_T	0.973270	0.973287	0.975964

Table 1: Comparison of the growth rates obtained from the DNS and the linear theory. Growth rate is the imaginary part of the temporal eigenvalue in the linear theory and it is calculated from the time history of the maximum amplitudes of the first Fourier modes in the azimuthal and axial directions from the DNS. $M = 2.0$, $Re = 2,000$, $R_1/R_2 = 0.5$, $T_2/T_1 = 1.0$, $\Omega_2/\Omega_1 = -1.0$, $\alpha = 19.0$.

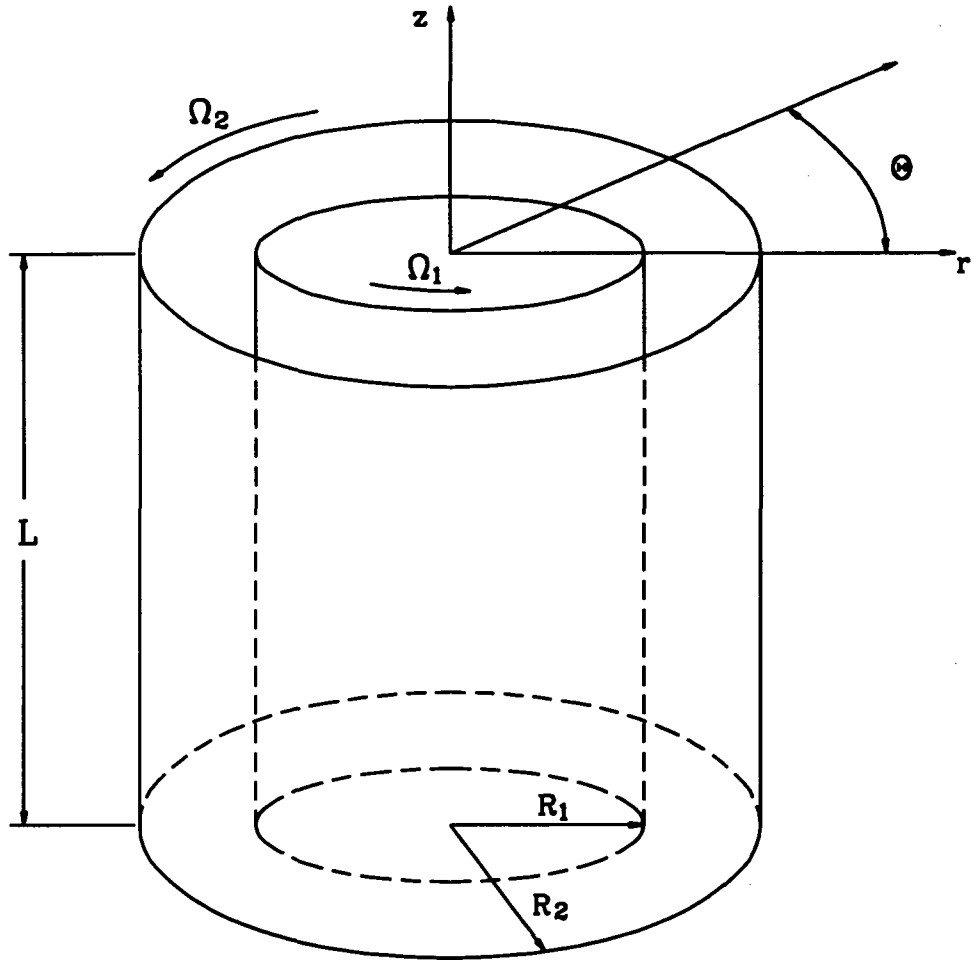

Figure 1: Coordinate system and the integration domain.

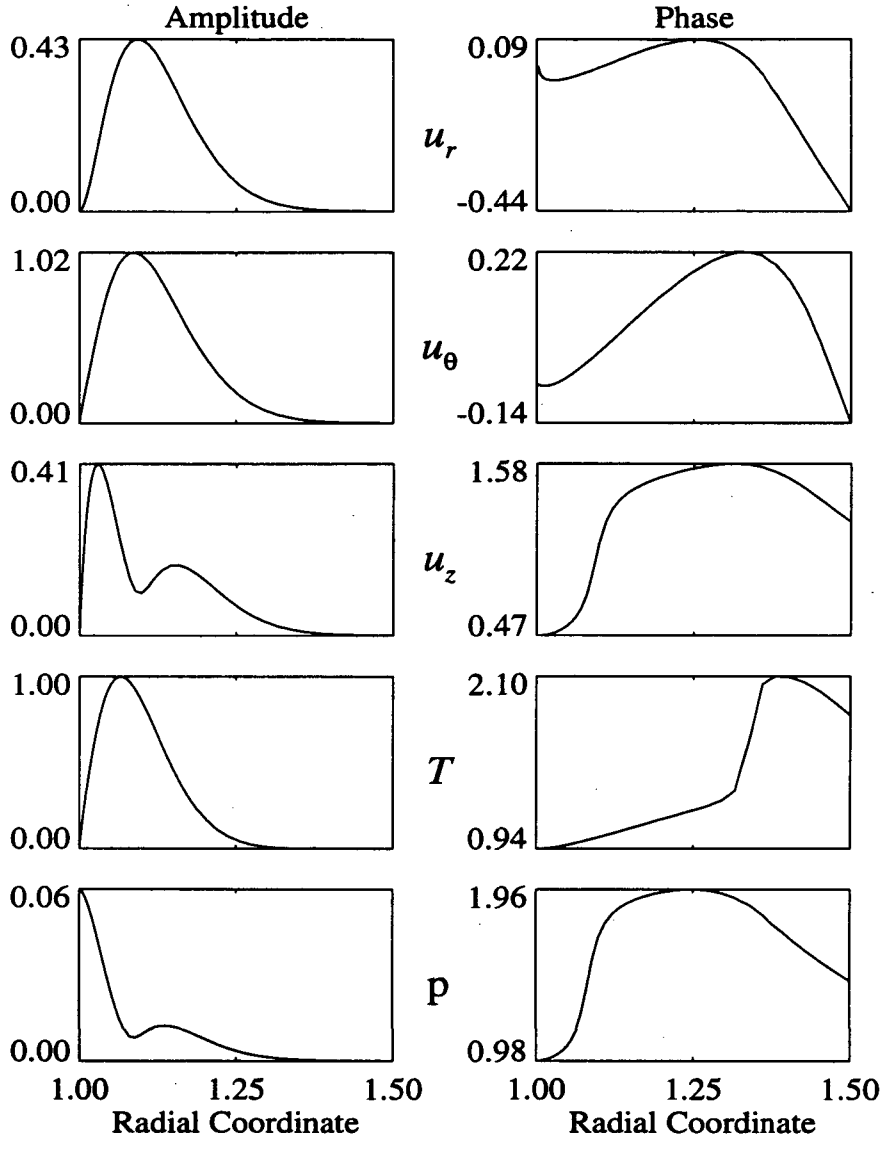

Figure 2: Radial distributions of the velocity, temperature, and pressure perturbation fields as obtained from the linear theory corresponding to the primary disturbance used in the case studies. Linear-theory prediction for the complex frequency is $\omega = 0.5168 + i0.9758$.

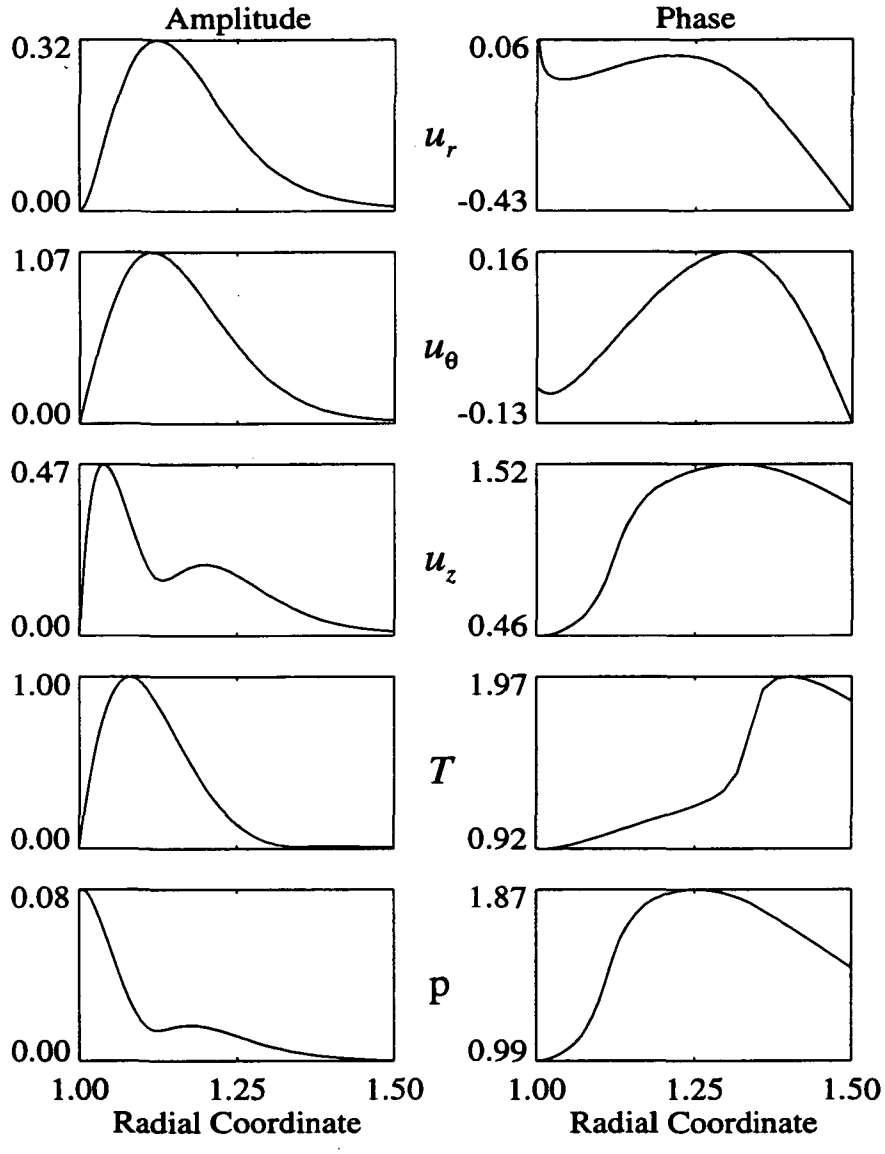

Figure 3: Radial distributions of the velocity, temperature, and pressure perturbation fields as obtained from the linear theory corresponding to the axial-subharmonic disturbance used in the case studies. Linear-theory prediction for the complex frequency is $\omega = 0.4517 + i0.7582$.

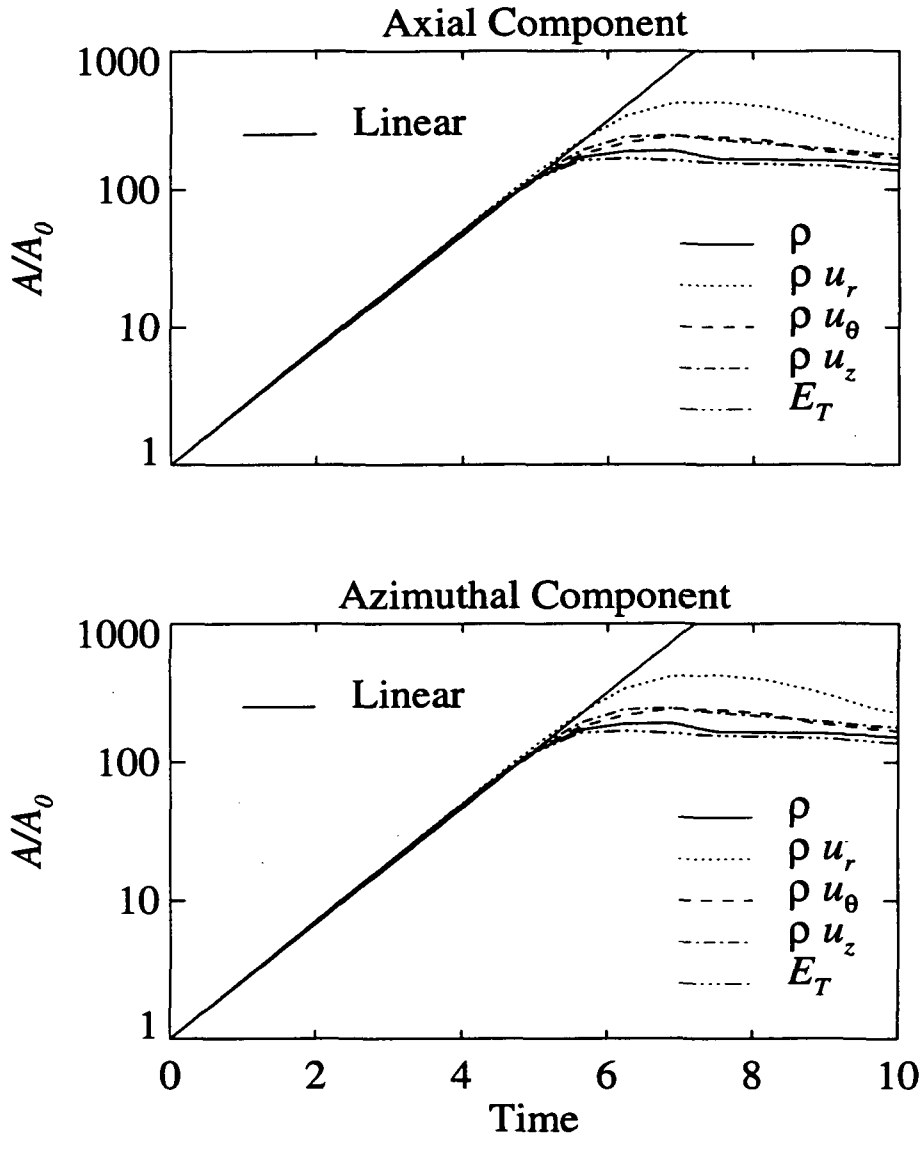

Figure 4: Initial exponential growth of the maximum amplitudes of the first Fourier modes of the flow variables during the direct numerical simulations for the harmonic evolution. Thick straight line is the prediction by the linear theory. $M = 2.0$, $Re = 2,000$, $R_1/R_2 = 0.5$, $T_2/T_1 = 1.0$, $\Omega_2/\Omega_1 = 0.0$, $\alpha = 19.0$, $Initial Amplitude = 0.001$.

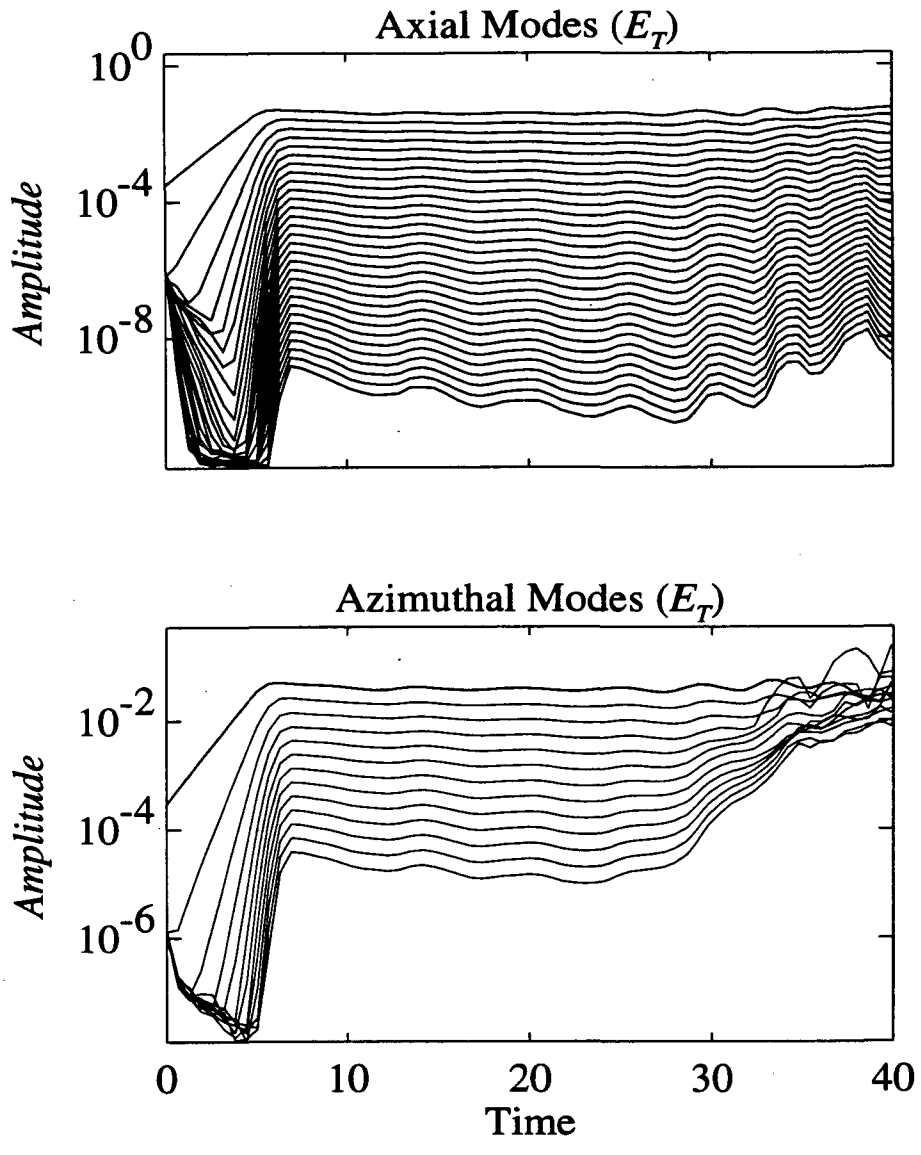

Figure 5: Temporal evolution of maximum Fourier amplitudes of harmonics in the axial and azimuthal direction. $M = 2.0$, $Re = 2,000$, $R_2/R_1 = 0.5$, and $\Omega_2/\Omega_1 = -1.0$.

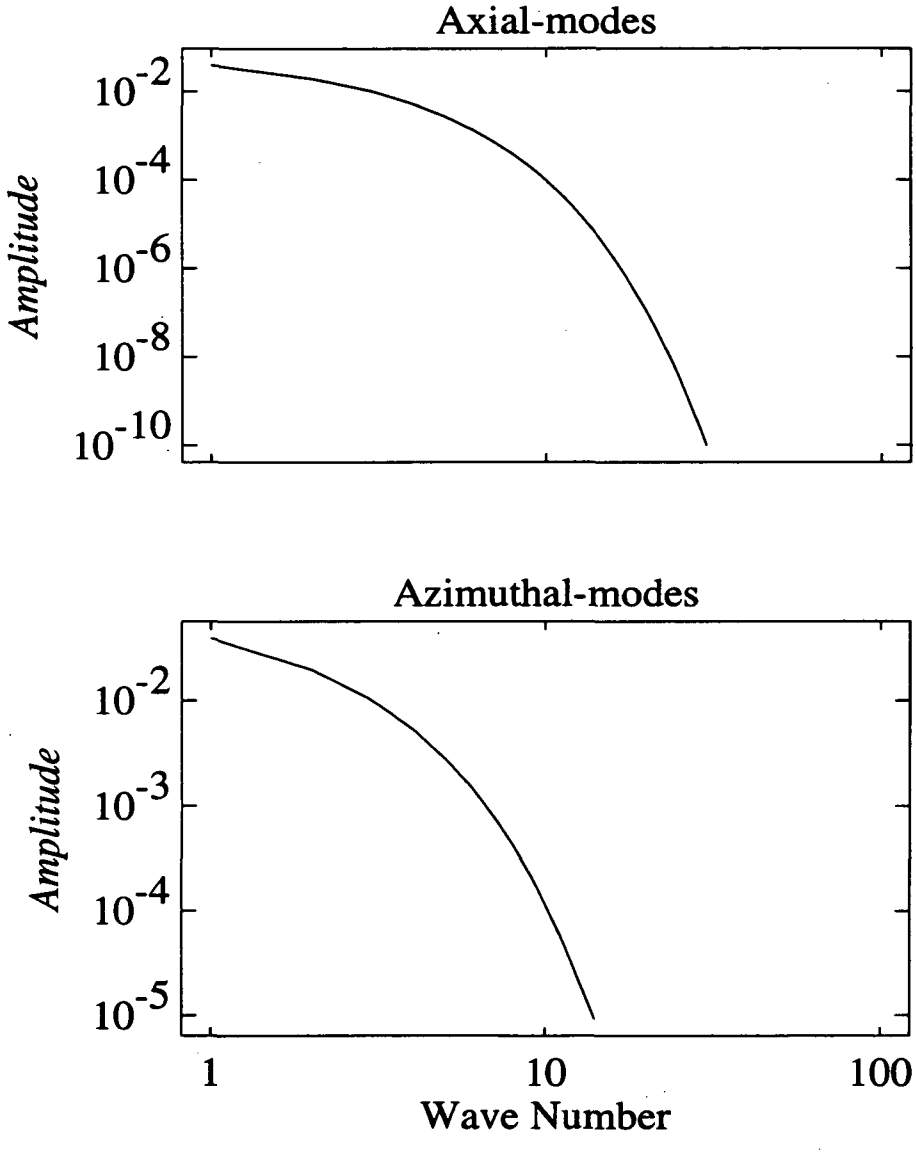

Figure 6: Energy spectra of maximum Fourier amplitudes of harmonics at time=25.51.

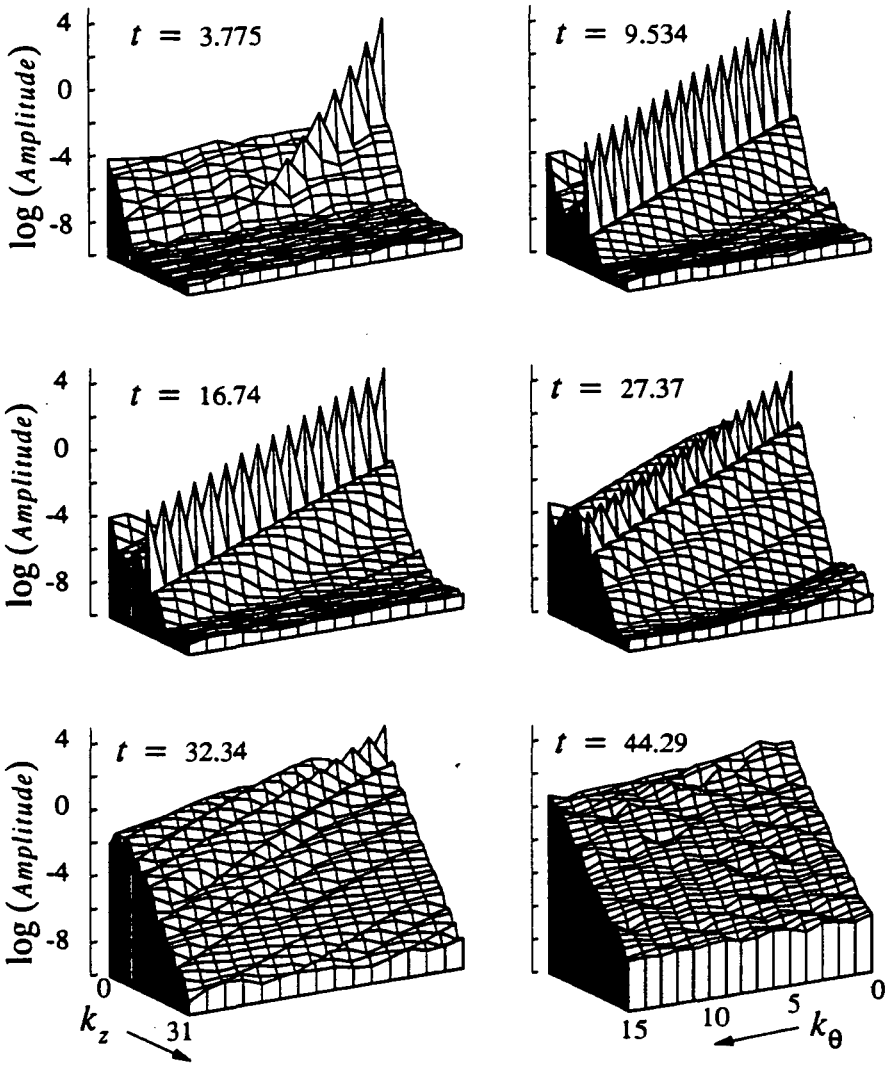

Figure 7: Amplitudes of two-dimensional Fourier modes in the harmonic case at different times.

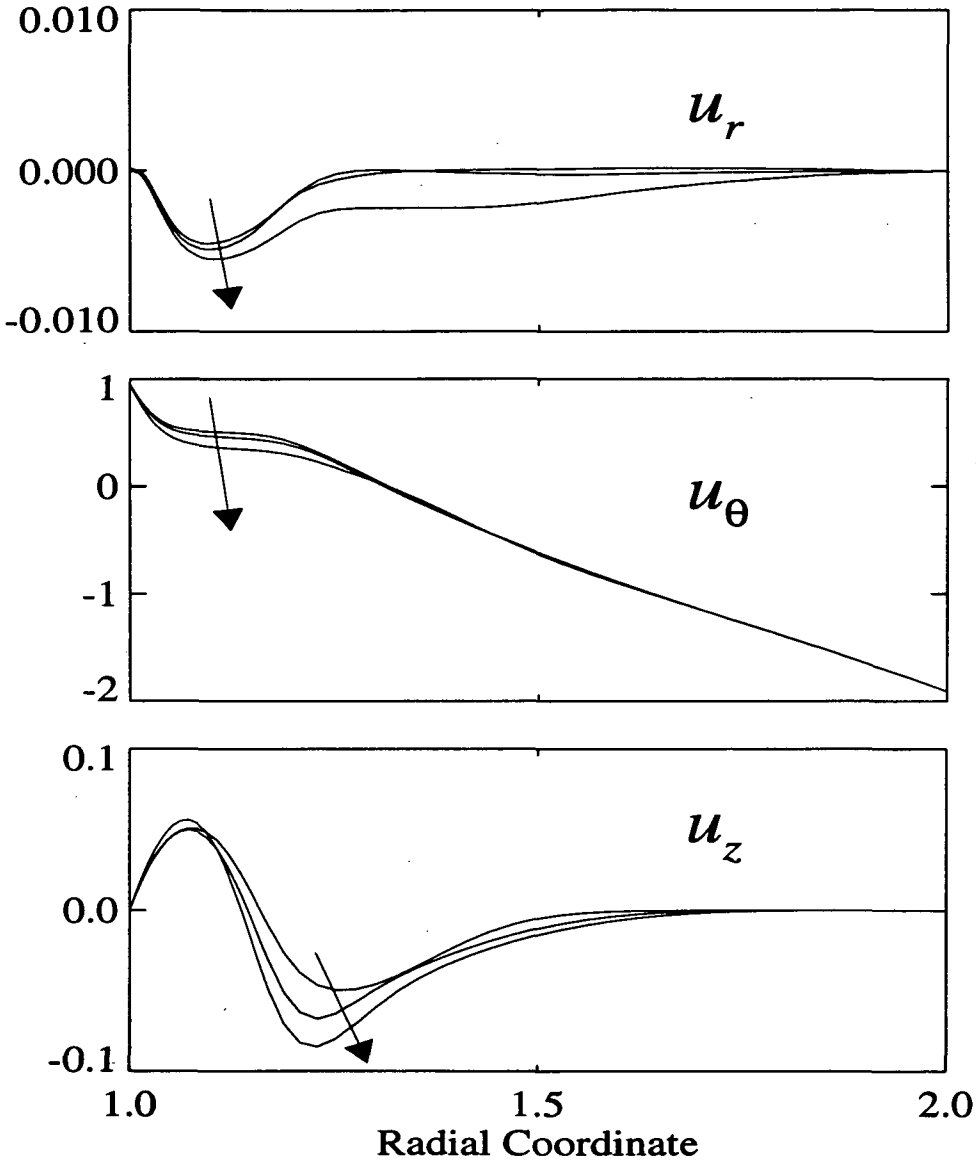

Figure 8: Evolution of the mean velocities in the harmonic case for $t = 12.85, 19.27, 25.51$ in the direction of the arrows.

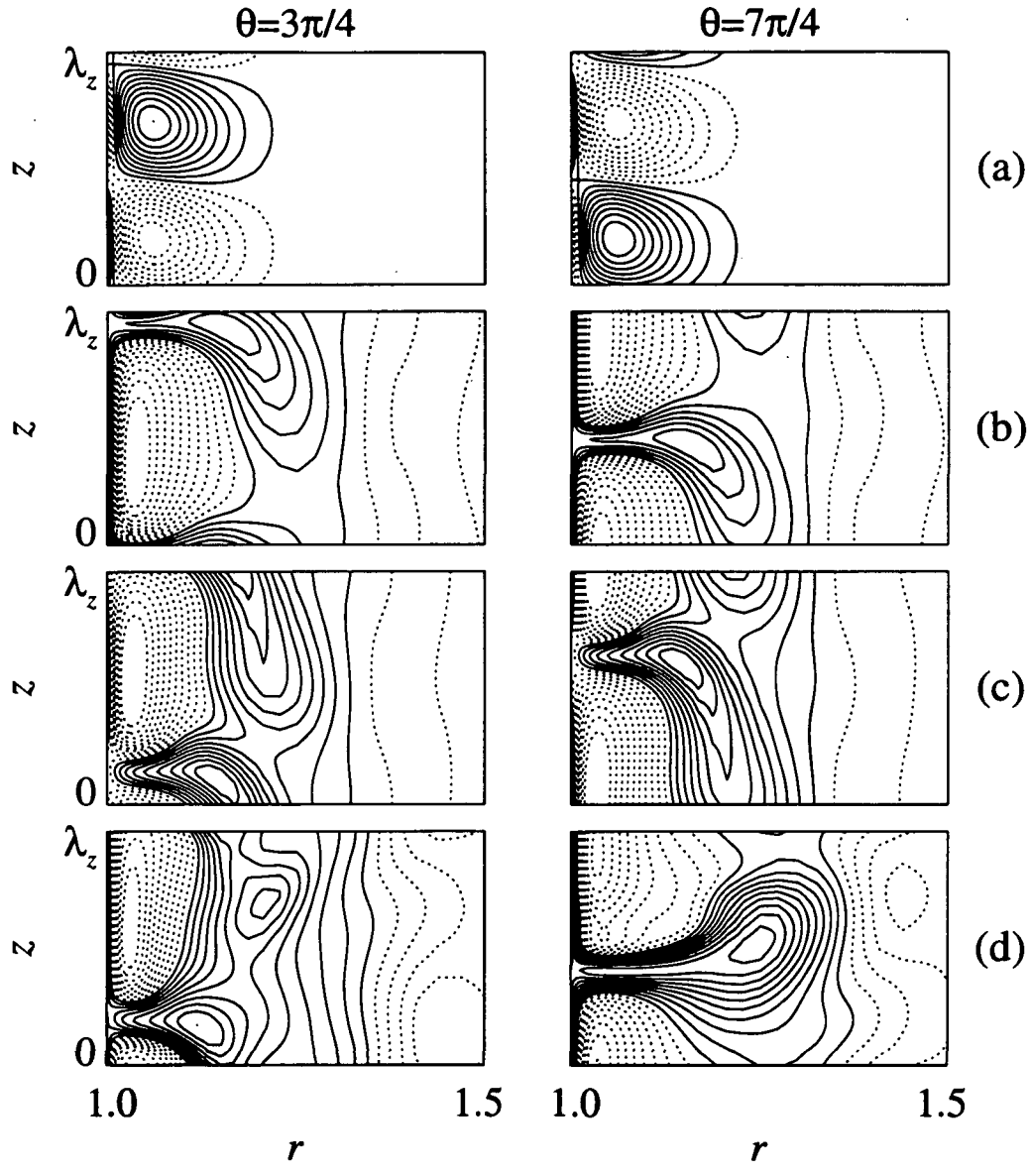

Figure 9: Contours of E_T at two different cross-sections of (r, z) plane at $t =$ 0.6313 (a), 12.85 (b), 25.51 (c), 38.00 (d). Contour levels are kept the same in (b), (c) and (d). Solid lines are used for positive levels and dotted lines for negative levels. Only inner half of the channel is shown for clarity.

Figure 10: Isosurfaces of 50% of the maximum of the disturbance total energy, E_T, at different times during the harmonic case. Only the domain $1.1 < r < 1.5$ is shown for clarity.

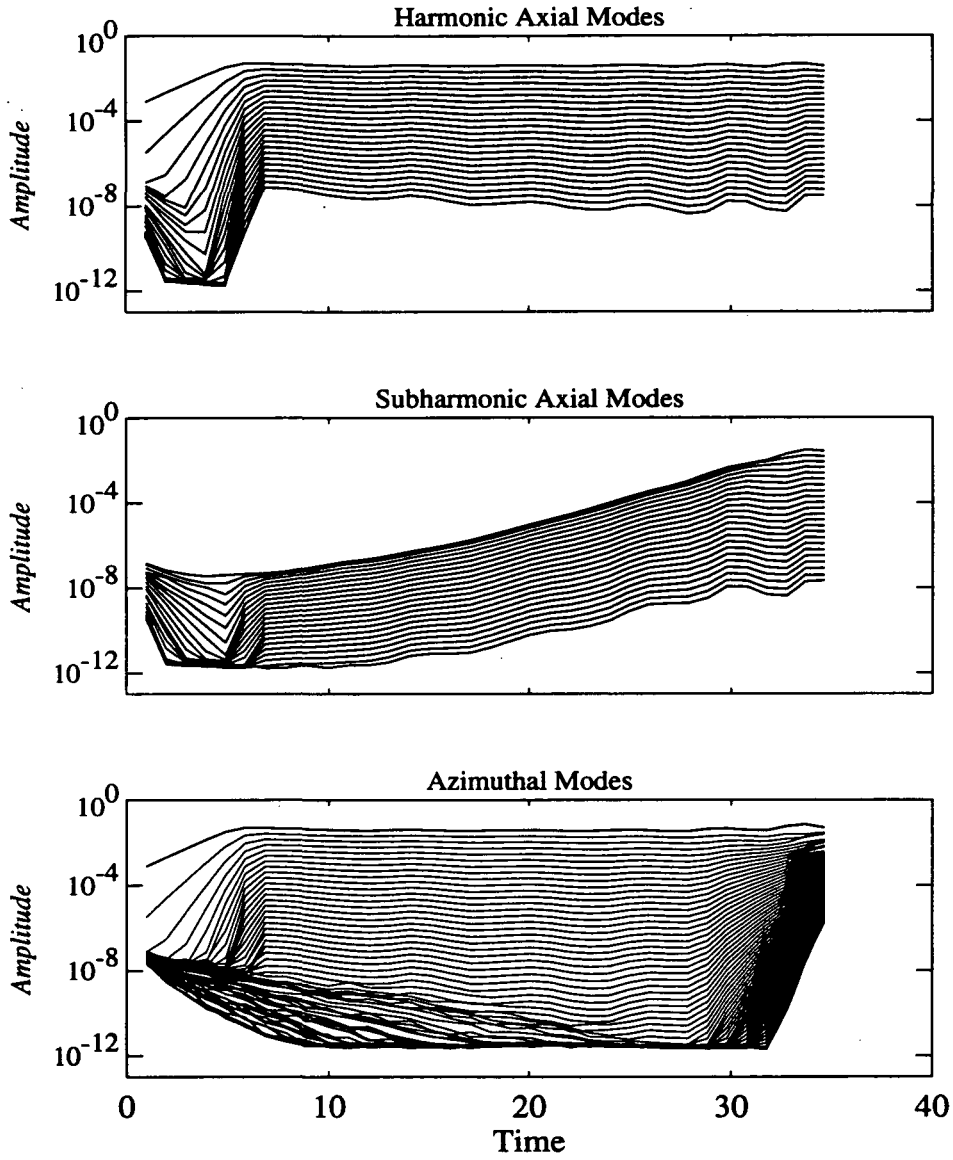

Figure 11: Temporal evolution of maximum Fourier amplitudes for the subharmonic case.

$$(N_r, N_\theta, N_z) = (81 \times 130 \times 102)$$

$$(N_r, N_\theta, N_z) = (65 \times 66 \times 102)$$

Figure 12: Comparison of spectral time evolution of the axial-harmonic modes up to $t = 21$ at two different spatial resolutions for the subharmonic case. $(N_r, N_\theta, N_z) = (65 \times 66 \times 102)$ case was terminated at $t = 21$.

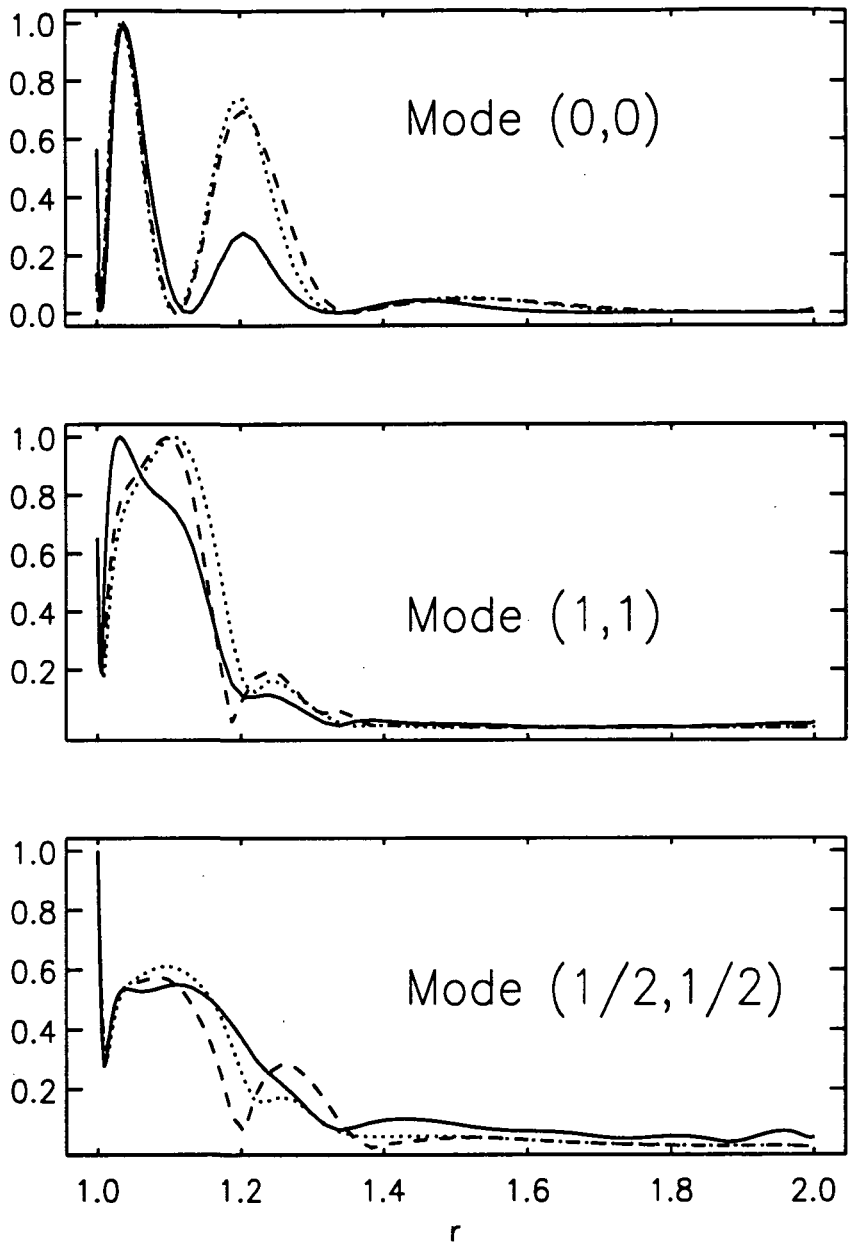

Figure 13: Radial Fourier amplitude distributions for the mean flow, fundamental mode, and the first subharmonic mode. ——— , $t = 15.10$, ····· , $t = 24.95$, – – – , $t = 29.79$.

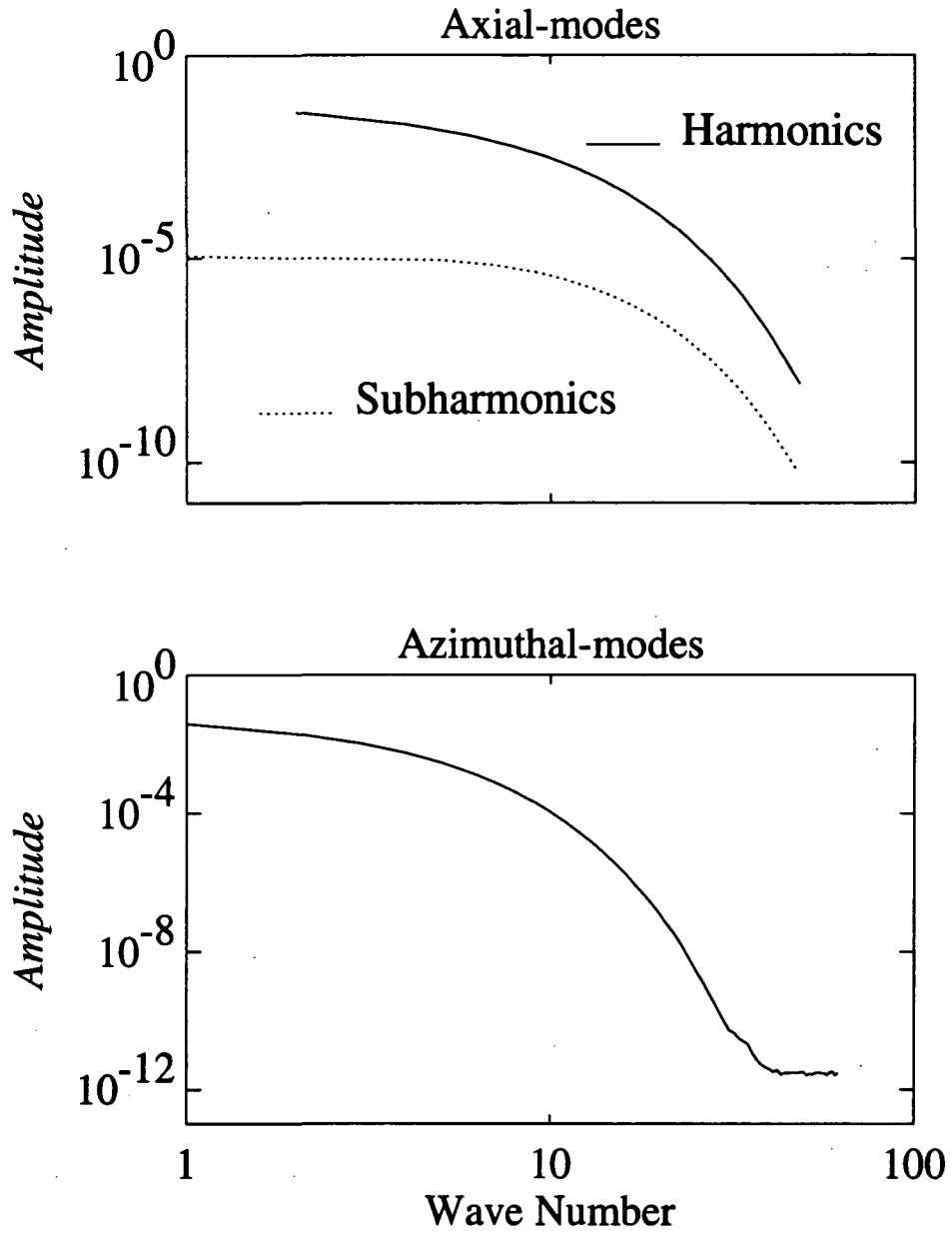

Figure 14: Energy spectra of maximum Fourier amplitudes in the subharmonic case at time = 20.07.

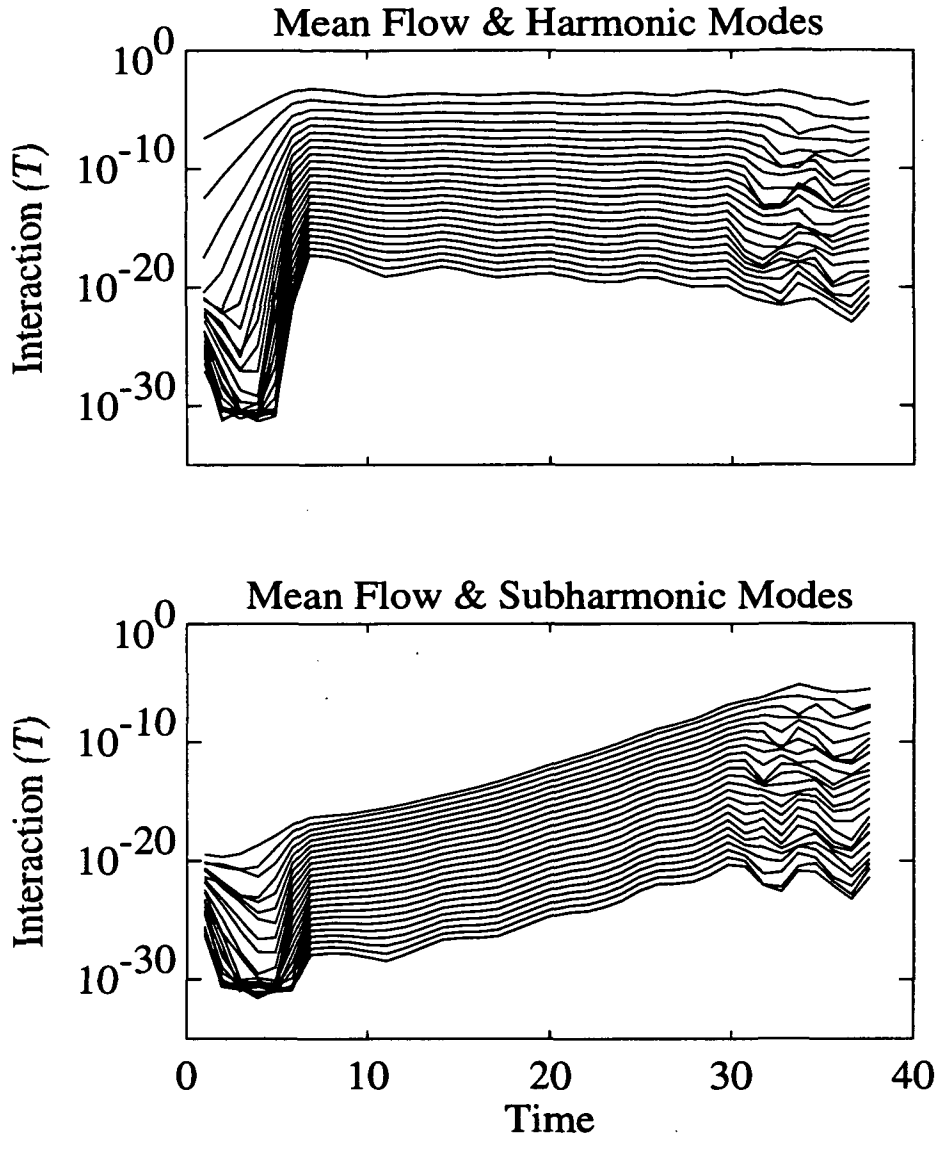

Figure 15: Temporal evolution of the energy transfer rate amplitude ($\boldsymbol{T}$in Eq. 24) from the mean flow ($k_1 = k_2 = 0$) to the various modes (k_1', k_2') with increasing wavenumbers from top to bottom in each plot.

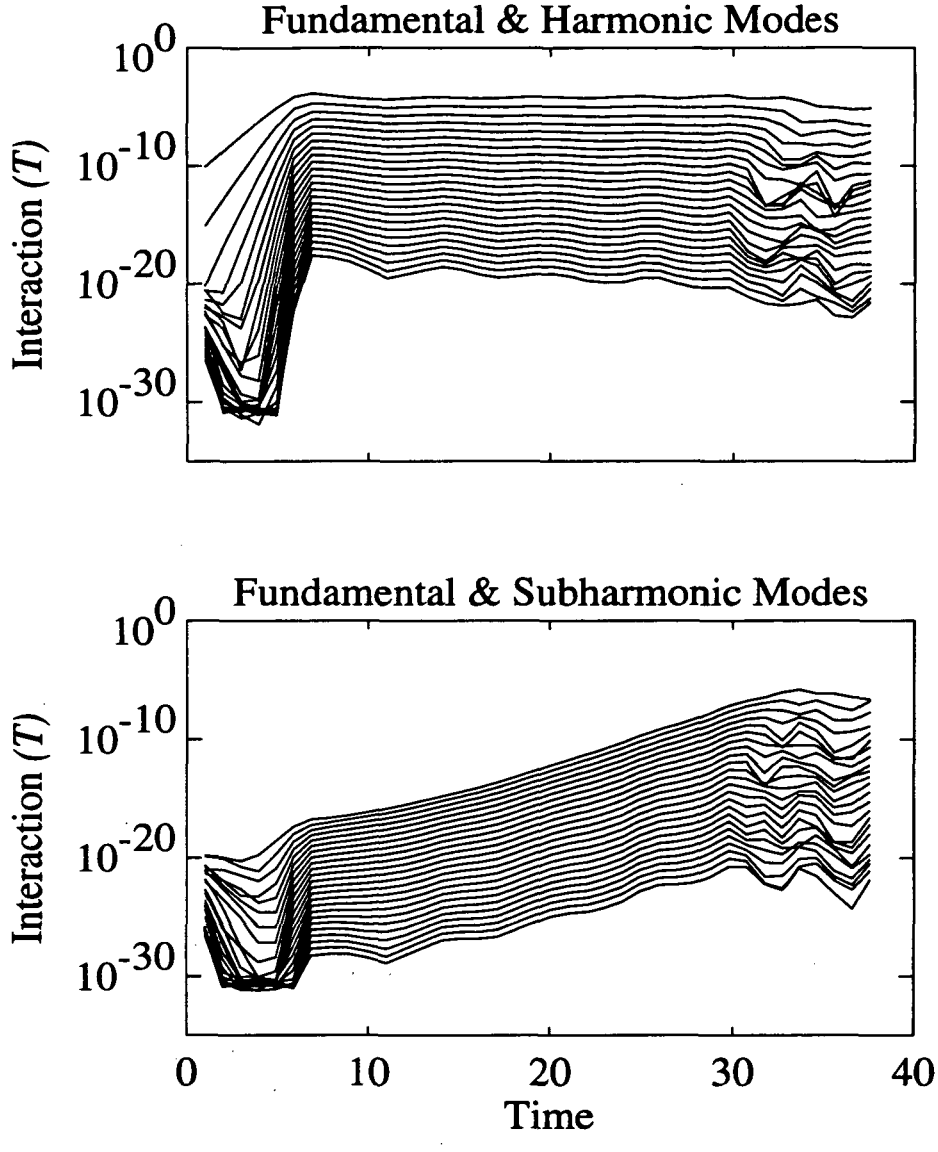

Figure 16: Temporal evolution of the energy transfer rate amplitude ($\boldsymbol{T}$in Eq. (24) from the fundamental mode ($k_1 = k_2 = 1$) to the various modes (k_1', k_2') with increasing wavenumbers from top to bottom in each plot.

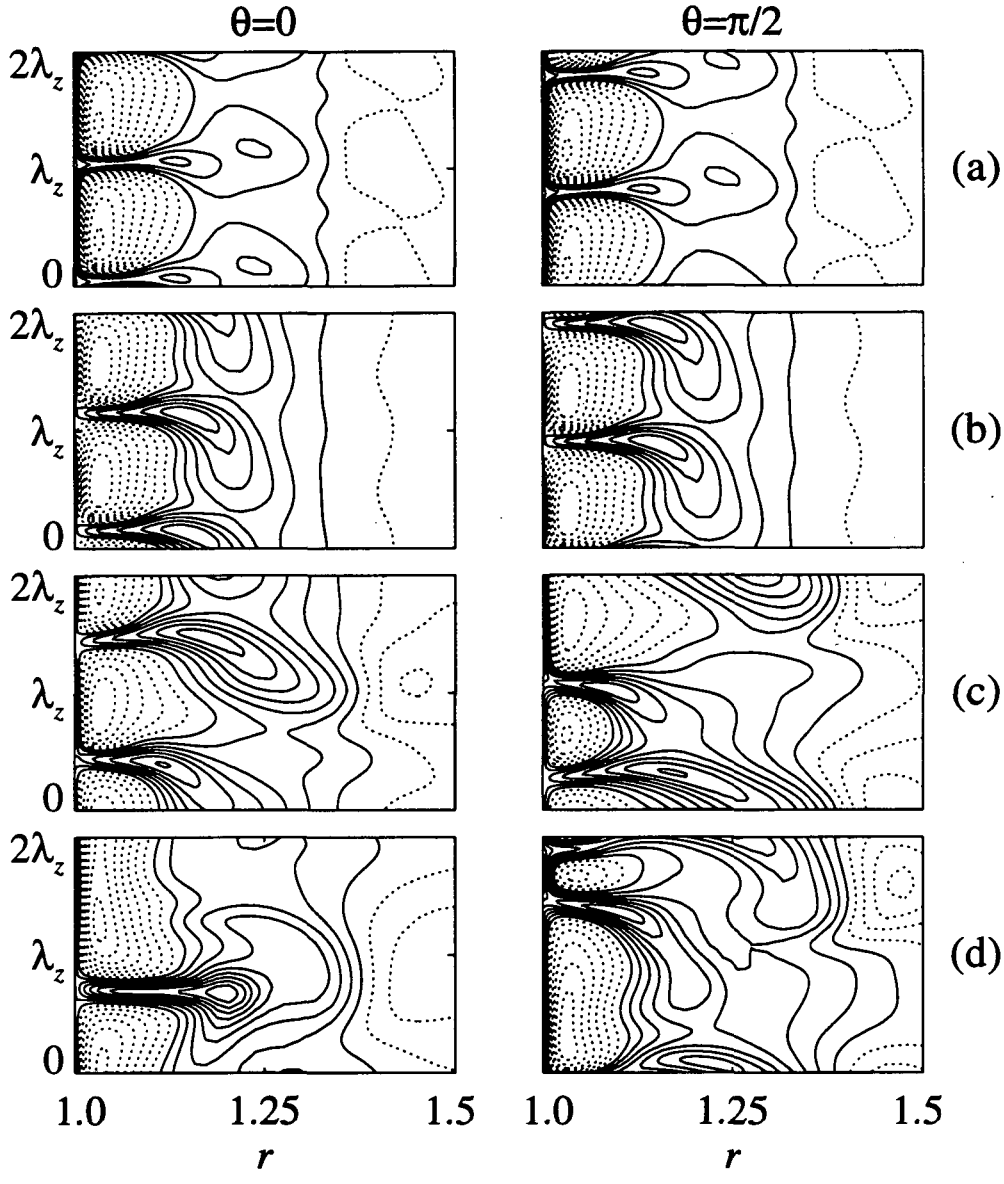

Figure 17: Contours of E_T in the subharmonic case at two different cross-sections of (r, z) plane at $t = 11.00$ (a), 21.01 (b), 30.76 (c), 35.64 (d). Contour levels are kept the same in all frames. Solid lines are used for positive levels and dotted lines for negative levels. Only inner half of the channel is shown for clarity.

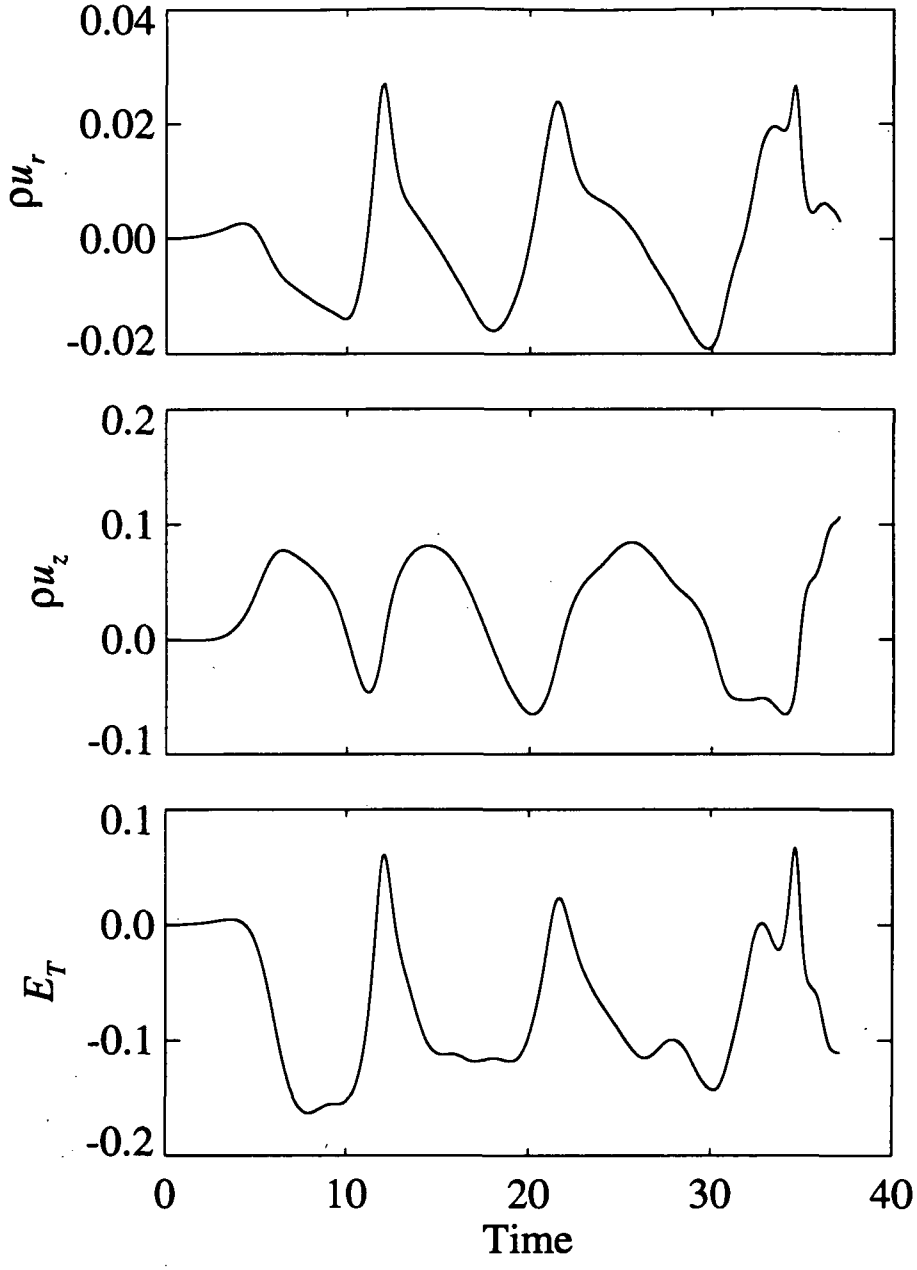

Figure 18: Time history data collected at the fixed point $(r, \theta, z) = (1.02, 0.0, \lambda_z/4)$.

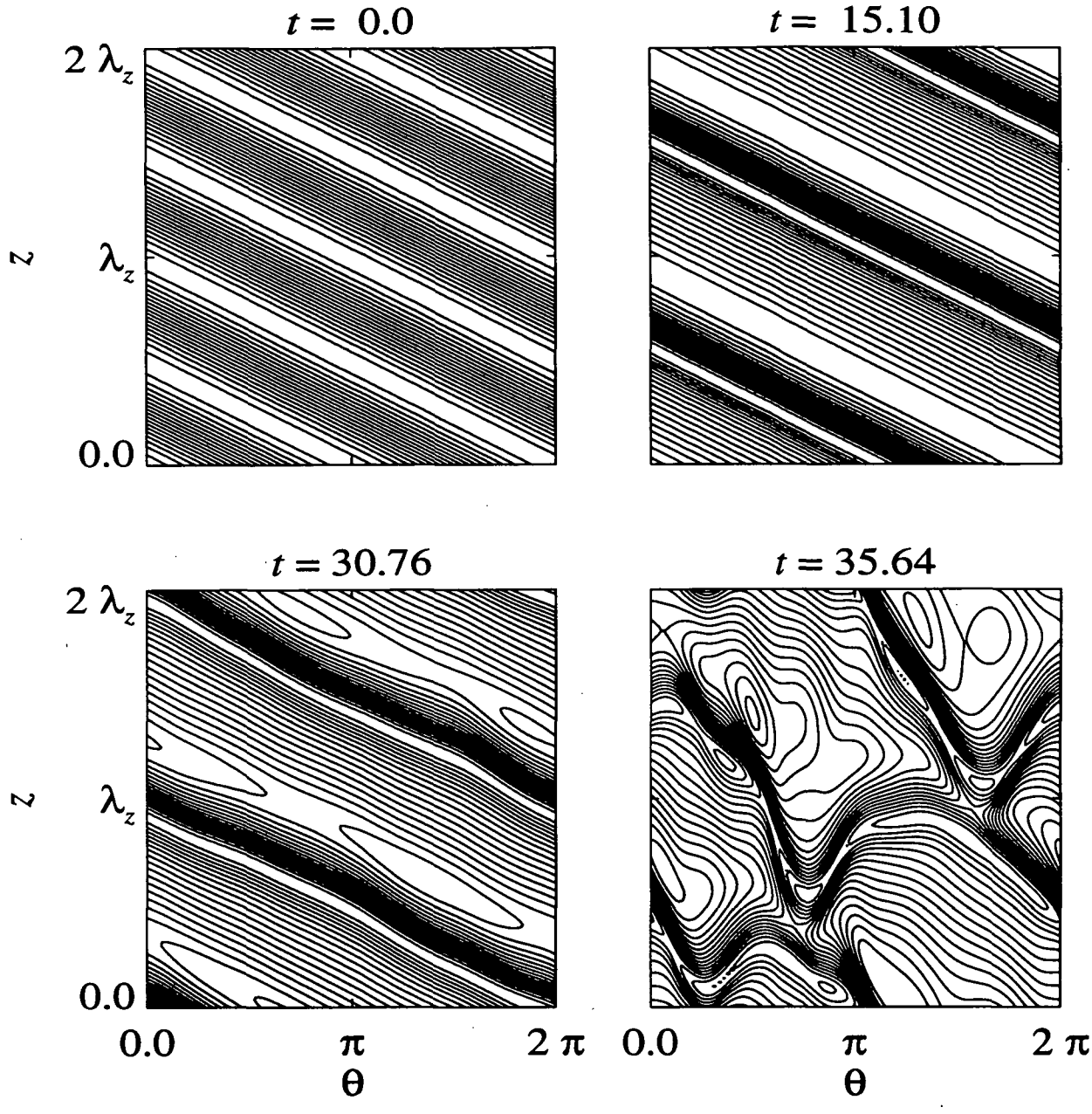

Figure 19: Contour plots of $\mu \partial u_\theta / \partial r$ in (z-θ) plane on the inner cylinder during the subharmonic-development case.

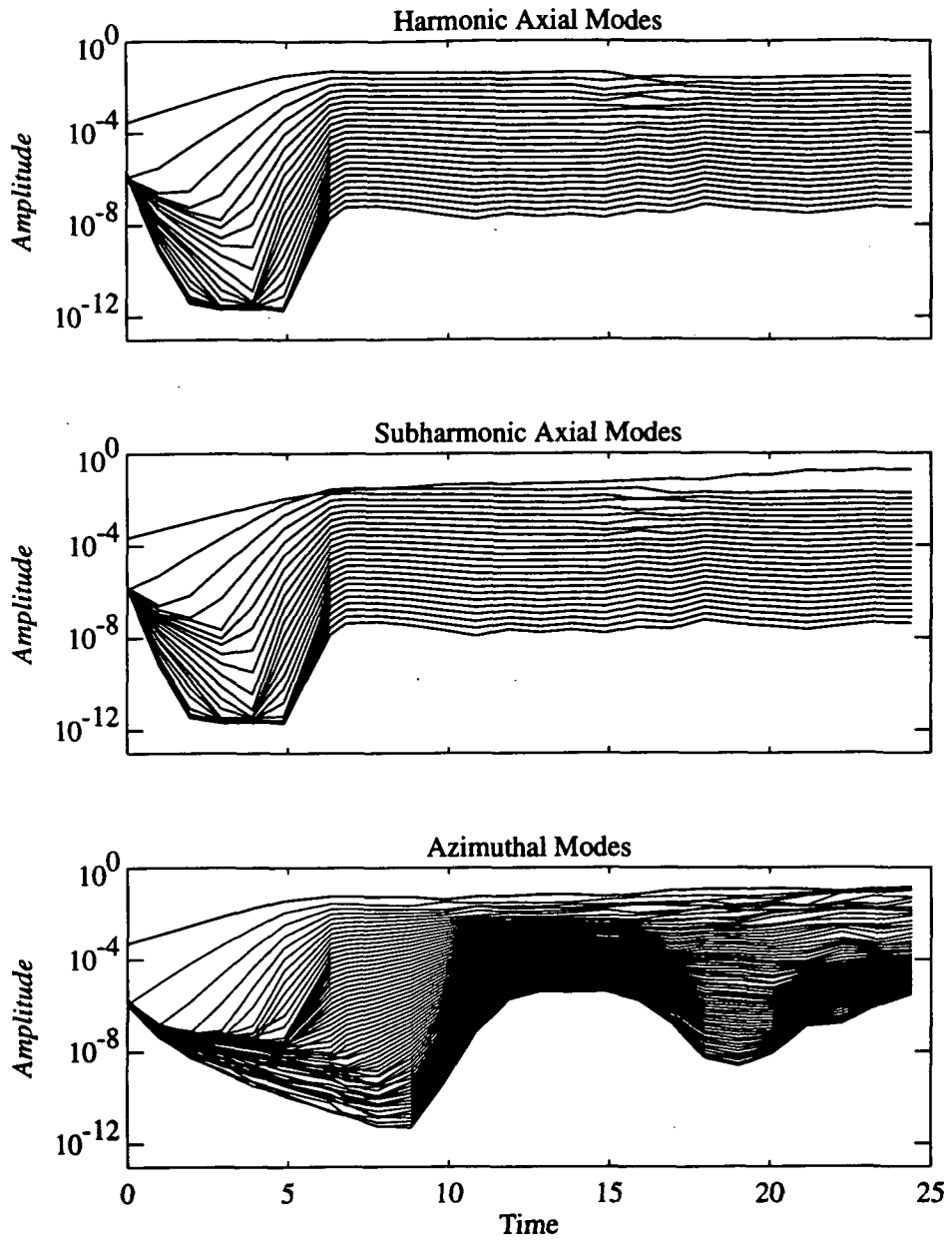

Figure 20: Temporal evolution of maximum Fourier amplitudes for the forced-subharmonic case.

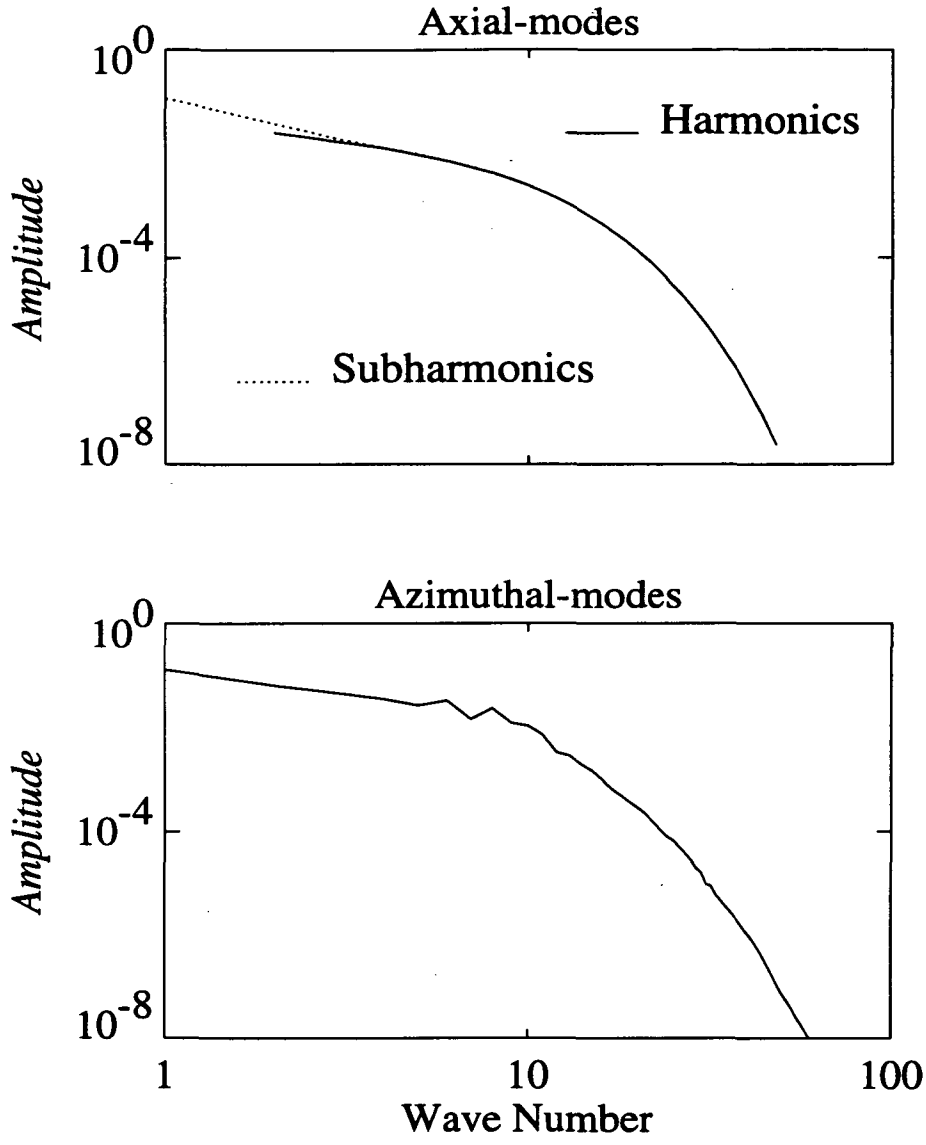

Figure 21: Energy spectra of maximum Fourier amplitudes in the forced-subharmonic case at time = 20.10.

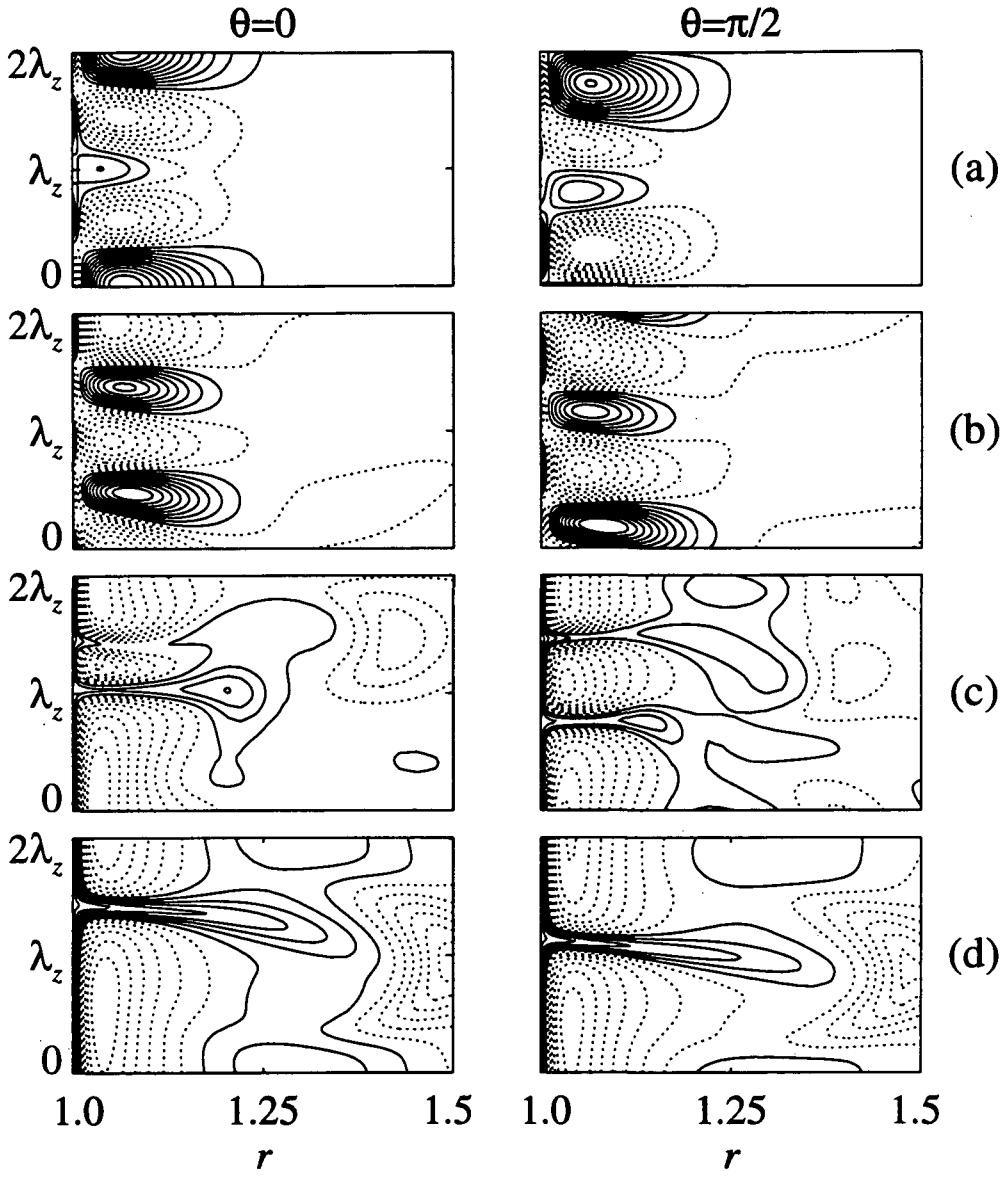

Figure 22: Contours of E_T in the forced-subharmonic case at two different cross-sections of (r, z) plane at $t = 0.0030$ (a), 4.888 (b), 9.844 (c), 14.87 (d). Contour levels are kept the same in (c) and (d). Solid lines are used for positive levels and dotted lines for negative levels. Only inner half of the channel is shown for clarity.

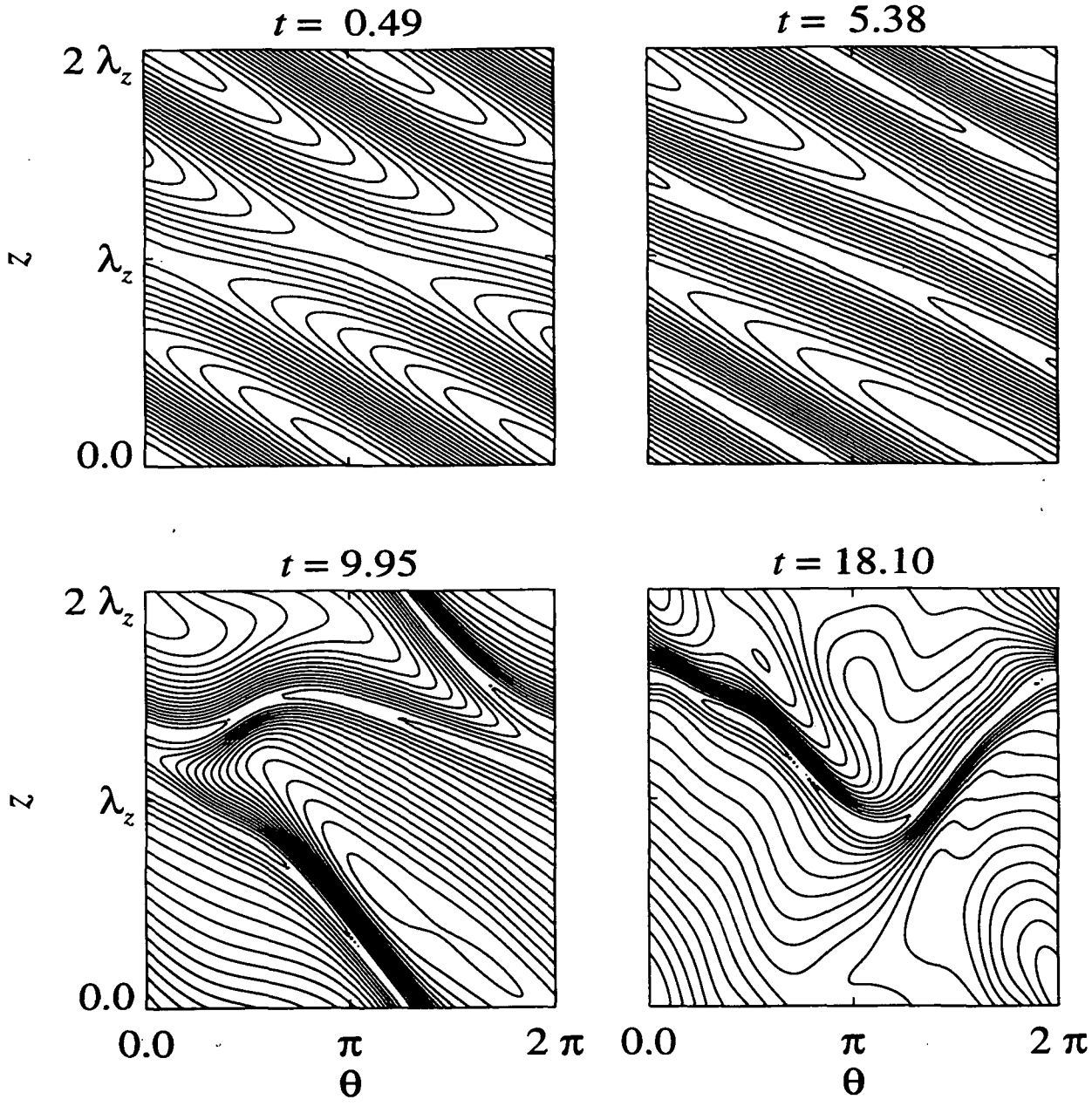

Figure 23: Contour plots of $\mu \partial u_\theta / \partial r$ in (z-θ) plane on the inner cylinder during the forced-subharmonic-development case.